Nonlinear aircraft sensor fault reconstruction in the presence of disturbances validated by real flight data

Lu, P; van Kampen, EJ; de Visser, CC; Chu, QP

DOI
10.1016/j.conengprac.2016.01.012

Publication date
2016

Document Version
Accepted author manuscript

Published in
Control Engineering Practice

Nonlinear aircraft sensor fault reconstruction in the presence of disturbances validated by real flight data

Peng Lu[a,*], Erik-Jan van Kampen[a], Cornelis de Visser[a], Qiping Chu[a]

[a]*Delft University of Technology, Kluyverweg 1, 2629HS Delft, The Netherlands*

Abstract

This paper proposes an approach for Inertial Measurement Unit sensor fault reconstruction by exploiting a ground speed-based kinematic model of the aircraft flying in a rotating earth reference system. Two strategies for the validation of sensor fault reconstruction are presented: closed-loop validation and open-loop validation. Both strategies use the same kinematic model and a newly-developed Adaptive Two-Stage Extended Kalman Filter to estimate the states and faults of the aircraft. Simulation results demonstrate the effectiveness of the proposed approach compared to an approach using an airspeed-based kinematic model. Furthermore, the major contribution is that the proposed approach is validated using real flight test data including the presence of external disturbances such as turbulence. Three flight scenarios are selected to test the performance of the proposed approach. It is shown that the proposed approach is robust to model uncertainties, unmodelled dynamics and disturbances such as time-varying wind and turbulence. Therefore, the proposed approach can be incorporated into aircraft Fault Detection and Isolation systems to enhance the performance of the aircraft.

Keywords: Fault reconstruction, Aircraft sensor faults, Real flight test data, Disturbances, Wind shear, Turbulence, Adaptive Two-Stage Extended Kalman Filter

*Corresponding author.

Email addresses: `P.Lu-1@tudelft.nl` (Peng Lu), `E.vanKampen@tudelft.nl` (Erik-Jan van Kampen), `c.c.devisser@tudelft.nl` (Cornelis de Visser), `q.p.chu@tudelft.nl` (Qiping Chu)

Nomenclature

FDI	Fault Detection and Isolation
FTC	Fault-Tolerant Control
IMU	Inertial Measurement Unit
IOTSEKF	Iterated Optimal Two-Stage Extended Kalman Filter
ATSEKF	Adaptive Two-Stage Extended Kalman Filter
KM	kinematic model
AS-KM	airspeed-based kinematic model
GS-KM	ground speed-based kinematic model
RMSE	root mean square error
SMO	Sliding Mode Observer
A_x, A_y, A_z	specific forces along the body axis, m/s^2
U_N, U_E, U_D	ground speed components in the local navigation frame, m/s
p, q, r	roll, pitch and yaw rates along the body axis, rad/s
u_a, v_a, w_a	airspeed components along body axis, m/s
u_w, v_w, w_w	wind speed components along earth axis, m/s
V	true airspeed, m/s
α, β	angle of attack, sideslip angle, rad
ϕ, θ, ψ	roll, pitch and yaw angles along the body axis, rad
$\boldsymbol{x}$, $\hat{\boldsymbol{x}}$	state and state estimate
$\boldsymbol{f}^i$, $\hat{\boldsymbol{f}}^i$	IMU sensor fault and its estimate
f_{A_x}, f_{A_y}, f_{A_z}	faults in the accelerometers, m/s^2
f_p, f_q, f_r	faults in the rate gyros, rad/s
k	time step
n, b, m	dimensions of the state, input, output respectively

1. Introduction

Sensor Fault Detection and Isolation (FDI) is important to enhance the performance of the aircraft. For future aircraft, structural optimization is important [1]. Model-based sensor FDI can substantially decrease the weight of the aircraft, which in turn increases the performance of the aircraft and leads to fuel and noise reduction [1]. During the last few decades, many approaches are proposed to detect and estimate sensor faults by making use of the model information [2, 3, 4, 5]. Projects related to FDI in aerospace engineering, the REconfiguration of CONtrol in Flight for Integral Global Upset REcovery (RECONFIGURE) [6] and Advanced Fault Diagnosis for Sustainable Flight Guidance and Control (ADDSAFE) project [1], also consider sensor faults. Recently, various model-based approaches have been proposed to deal with aircraft sensor faults. Marcos et al.[7] and Freeman et al. [8] use H_∞ to detect and isolate the sensor faults. Unknown input observers [9] are also applied to detect and isolate the sensor faults. Castaldi et al. [10, 11] propose a geometric approach for the FDI of aircraft sensors. Sliding Mode Observers (SMOs) [12, 13] are used to reconstruct the sensor faults. Control-based FDI method, which makes use of the control information, is also proposed [14]. Multiple-Model Adaptive Estimation approach is proposed in [15] to detect and estimate the aircraft sensor faults. For one thing, the performance of model-based approaches depends on the accuracy of the model used. Due to complexity, models of real-life systems are normally simplifications with limited accuracy. For aircraft dynamic models, exact aerodynamic forces and moments are difficult to obtain which leads to model uncertainties. For another, most systems are subject to external disturbances which will further affect the performance of model-based approaches. In civil aviation, wind and even time-varying wind is unavoidable during flight. One of the biggest challenges for aircraft FDI is the presence of disturbances such as time-varying wind and turbulence. Wind and turbulence can be present in various circumstances during the flight. As such, FDI approaches more robust to model uncertainties and disturbances are favored in aerospace engineering.

This paper considers the fault reconstruction of the Inertial Measurement Unit (IMU) sensors. The IMU contains accelerometers which measure the specific forces (A_x, A_y and A_z) and rate gyros which measure the angular rates (p, q and r) of the aircraft. The ADDSAFE project also considers faults in the yaw rate (r) sensor [12, 16]. Alwi and Edwards [12] use a Linear Parameter Varying sliding mode scheme to reduce the influence of linearization errors. Van Eykeren and Chu [16] use an airspeed-based kinematic model (AS-KM) of the aircraft which does not require linearization. Another advantage of using the AS-KM is that it does not require the calculation of the aerodynamic forces and moments. Since exact aerodynamic forces and moments are difficult to obtain, using the kinematic model reduces the effect of model uncertainties for FDI. Many approaches are proposed for the aircraft sensor FDI using this AS-KM, such as Double-Model Adaptive Estimation [17], Sliding Mode Differentiator [16] and Adaptive Three-Step Unscented Kalman Filter [18]. Van Eykeren and Chu [16] and Lu et al. [15] use the same kinematic model (KM) for the fault estimation of the IMU sensors. The limitation of their approach is that the influence of disturbances such as turbulence is not considered. In Lu et al. [19], the turbulence influence is considered by a ground speed-based KM. The approach is validated by only simulation which demonstrates that the proposed FDI approach is less sensitive to turbulence.

Regarding the validation of aircraft sensor FDI approaches, the validation using real flight data is important. The performance of sensor FDI approaches is more reliable if they are validated by real flight tests or real flight test data. For real flights, sensors may not behave as in the simulations. More importantly, during real flight tests, various realistic wind and turbulence conditions can be experienced. Although in some circumstances the wind can be approximately constant, the wind is normally time varying. Moreover, turbulence can be encountered in various situations during the flight. These flight conditions can test the performance of the FDI approaches in the presence of external disturbances. Therefore, use of real flight test data containing different flight conditions, especially wind and turbulent conditions, is necessary to validate the performance of model-based FDI approaches.

Few researchers [20, 21, 19] validate the IMU sensor fault detectors using real flight data. Berdjag et al. [20, 22] detect oscillatory faults [23] of three inertial sensors. Their approach is validated on a real flight data set. Hu and Seiler [21] assess the false alarm probability of a model-based Unmanned Aerial Vehicle fault detection system. Lu et al. [19] also used real flight test data to validate the performance of model-based fault reconstruction for the IMU sensors. However, there are two limitations in [19]. Firstly, it assumes a flat and non-rotating earth which may introduce errors when long-range flights are considered. Furthermore, the real flight test in [19] contains no turbulence since the objective of the flight test was data acquisition for aerodynamic model identification [24, 19]. Therefore, the performance of the FDI approach in [19], in the presence of various disturbances such as time-varying wind and turbulence, is not validated.

In the present paper, an IMU sensor fault reconstruction approach using a general ground-speed-based kinematic model (GS-KM) is proposed. This KM, which is a model of the aircraft flying over a spherical and rotating earth, is proposed as the model for the IMU sensor fault reconstruction. Two validation strategies (open-loop and closed-loop validations) are implemented and compared for the IMU sensor fault reconstruction. Another contribution of this paper is that a new Adaptive Two-Stage Extended Kalman Filter (ATSEKF) is proposed to reconstruct the states and faults. This ATSEKF is an improved version of the Iterated Optimal Two-Stage Extended Kalman Filter (IOTSEKF) [19] with covariance matrix adaption. The performance of the ATSEKF for the sensor fault reconstruction is validated by simulation. The fault scenarios include not only biases, but also drift and oscillatory faults. All the IMU sensor faults are estimated in an unbiased sense. The performance using the GS-KM is compared with that using the AS-KM. The performance of the ATSEKF is also compared with existing approaches such as the SMO.

The major contribution of this paper is that the performance of the proposed IMU sensor fault reconstruction approach is validated using real flight test data in the presence of disturbances such as time-varying wind and turbulence. Several flight tests are performed in order to gather data in different flight conditions. Zero-g flight is also performed in order to test the performance of the approach over a wide range of the flight envelope. Flight data in turbulent conditions is also collected which will test the performance in the presence of strong external disturbances. The validation is performed using three different flight conditions: level flight, zero-g and turbulence. The performance of using the GS-KM is compared to the approach using the AS-KM in order to demonstrate the superiority of the proposed approach. Furthermore, the results sufficiently demonstrate that the proposed approach is suitable for IMU sensor fault reconstruction in practice.

The structure of this paper is as follows: Section 2 proposes an approach which uses a new KM for the IMU sensor fault reconstruction. Section 3 introduces the newly-developed ATSEKF for sensor fault reconstruction. Besides, two validation strategies are proposed which use the ATSEKF and the proposed KM. The performance of the proposed approach is demonstrated using simulated data. In Section 4, the three flight scenarios are introduced. Section 5 presents the real flight data validation results using the proposed approach in various flight and wind conditions. Section 6 concludes the paper.

2. Novel approach for IMU sensor fault reconstruction

This section proposes an approach for IMU fault reconstruction based on a GS-KM. For comparison, the previously used KM, the AS-KM [25, 26], is also presented.

2.1. Aircraft KMs including IMU sensor faults

The proposed GS-KM is a KM of the aircraft flying in a rotating earth reference frame [27]. It should be noted that this model has not been used for aircraft fault reconstruction.

The GS-KM including IMU sensor faults can be described as follows:

$$\dot{\boldsymbol{x}}(t) = \boldsymbol{f}(\boldsymbol{x}(t), \boldsymbol{u}_m(t), \boldsymbol{f}^i(t), t) + \mathbf{G}(\boldsymbol{x}(t))\boldsymbol{w}(t) \tag{1}$$

$$\boldsymbol{y}(t) = \boldsymbol{h}(\boldsymbol{x}(t)) \tag{2}$$

$$\boldsymbol{y}_m(t) = \boldsymbol{y}(t) + \boldsymbol{v}(t), \quad t = t_i, \ i = 1, 2, ... \tag{3}$$

where $\boldsymbol{x} \in \mathbb{R}^n$ represents the system states, $\boldsymbol{u}_m \in \mathbb{R}^b$ the measured input, $\boldsymbol{y}_m \in \mathbb{R}^m$ the measured output. The subscript 'm' indicates that the corresponding variable is measured. $\mathbf{G} \in \mathbb{R}^{n \times b}$ is the noise distribution matrix. The function $\boldsymbol{f}^i \in \mathbb{R}^b$ represents the input faults. The system equation variables are defined as follows:

$$\boldsymbol{x} = [U_N \ U_E \ U_D \ \phi \ \theta \ \psi]^T \tag{4}$$

$$\boldsymbol{u}_m = \ [A_{xm} \ A_{ym} \ A_{zm} \ p_m \ q_m \ r_m]^T \ = \boldsymbol{u}^0 + \boldsymbol{w} + \boldsymbol{f}^i \tag{5}$$

$$\boldsymbol{u}^0 = [A_x \ A_y \ A_z \ p \ q \ r \ ]^T \tag{6}$$

$$\boldsymbol{w} = [w_{Ax} \ w_{Ay} \ w_{Az} \ w_p \ w_q \ w_r \ ]^T \tag{7}$$

$$\boldsymbol{f}^i = [f_{Ax} \ f_{Ay} \ f_{Az} \ f_p \ f_q \ f_r]^T \tag{8}$$

$$\boldsymbol{y}_m = [U_{Nm} \ U_{Em} \ U_{Dm} \ \phi_m \ \theta_m \ \psi_m]^T \tag{9}$$

$$\boldsymbol{v} = [v_{U_N} \ v_{U_E} \ v_{U_D} \ v_\phi \ v_\theta \ v_\psi]^T \tag{10}$$

where the U_N, U_E and U_D are the ground speed velocity components in the local navigation frame. A_x, A_y and A_z are the specific forces, ϕ, θ and ψ are the Euler angles and p, q, r are the rotational rates. It should be noticed that $\boldsymbol{u}_m$ is the measurement of the IMU which contains faults $\boldsymbol{f}^i$. f_{Ax}, f_{Ay} and f_{Az} represent the faults in the accelerometers while f_p, f_q and f_r represent the faults in the rate gyros. $\boldsymbol{w}$ is the process noise sequence and $\boldsymbol{v}$ is the noise sequence in the output measurements denoted by $\boldsymbol{y}_m$.

For the GS-KM proposed in this paper, $\boldsymbol{f}(\boldsymbol{x}(t), \boldsymbol{u}_m(t), \boldsymbol{f}^i(t), t)$ is given as follows:

$$\begin{cases} (A_{xm} - f_{Ax})\mathrm{c}\theta\mathrm{c}\psi + (A_{ym} - f_{Ay})(\mathrm{s}\phi\mathrm{s}\theta\mathrm{c}\psi - \mathrm{c}\phi\mathrm{s}\psi) + (A_{zm} - f_{Az})(\mathrm{c}\phi\mathrm{s}\theta\mathrm{c}\psi + \mathrm{s}\phi\mathrm{s}\psi) \\ \quad + \dfrac{U_N U_D}{R_e + h} - \dfrac{U_E^2 \mathrm{t}\delta}{R_e + h} - 2\Omega U_E \mathrm{s}\delta \\ (A_{xm} - f_{Ax})\mathrm{c}\theta\mathrm{s}\psi + (A_{ym} - f_{Ay})(\mathrm{s}\phi\mathrm{s}\theta\mathrm{s}\psi + \mathrm{c}\phi\mathrm{c}\psi) + (A_{zm} - f_{Az})(\mathrm{c}\phi\mathrm{s}\theta\mathrm{s}\psi - \mathrm{s}\phi\mathrm{c}\psi) \\ \quad + \dfrac{U_N U_E \mathrm{t}\delta}{R_e + h} + \dfrac{U_E U_D}{R_e + h} + 2\Omega(U_N \mathrm{s}\delta + U_D \mathrm{c}\delta) \\ -(A_{xm} - f_{Ax})\mathrm{s}\theta + (A_{ym} - f_{Ay})\mathrm{s}\phi\mathrm{c}\theta + (A_{zm} - f_{Az})\mathrm{c}\phi\mathrm{c}\theta \\ \quad - \dfrac{U_N^2}{R_e + h} - \dfrac{U_E^2}{R_e + h} - 2\Omega U_E \mathrm{c}\delta + g \\ (p_m - f_p) + (q_m - f_q)\mathrm{s}\phi\mathrm{t}\theta + (r_m - f_r)\mathrm{c}\phi\mathrm{t}\theta - (\dfrac{U_E}{R_e + h} + \Omega\mathrm{c}\delta)\dfrac{\mathrm{c}\psi}{\mathrm{c}\theta} + \dfrac{U_N \mathrm{s}\psi}{(R_e + h)\mathrm{c}\theta} \\ (q_m - f_q)\mathrm{c}\phi - (r_m - f_r)\mathrm{s}\phi + (\dfrac{U_E}{R_e + h} + \Omega\mathrm{c}\delta)\mathrm{s}\psi + \dfrac{U_N \mathrm{c}\psi}{R_e + h} \\ (q_m - f_q)\dfrac{\mathrm{s}\phi}{\mathrm{c}\theta} + (r_m - f_r)\dfrac{\mathrm{c}\phi}{\mathrm{c}\theta} + (\dfrac{U_E}{R_e + h} + \Omega\mathrm{c}\delta)\mathrm{t}\theta\mathrm{c}\psi + \dfrac{U_N \mathrm{t}\theta\mathrm{s}\psi}{R_e + h} + \dfrac{U_E \mathrm{t}\delta}{R_e + h} + \Omega\mathrm{s}\delta \end{cases} \tag{11}$$

where s(•), c(•) and t(•) denote the trigonometric functions sin(•), cos(•) and tan(•) respectively. $R_e = 6367$ km, $\Omega = 7.2921 \times 10^{-5}$ rad/s, δ is the latitude and h is the altitude. The gravity acceleration g is calculated as follow [27]:

$$g = 9.780318(\frac{R_e}{R_e + h})^2(1 + 5.3024 \times 10^{-3}\mathrm{s}^2\delta - 5.9 \times 10^{-6}\mathrm{s}^2 2\delta) \tag{12}$$

In Eq. (1), $\mathbf{G}(\boldsymbol{x}(t))$ is defined as follows:

$$\mathbf{G}(\boldsymbol{x}(t)) = \begin{bmatrix} -\mathrm{c}\theta\mathrm{c}\psi & -(\mathrm{s}\phi\mathrm{s}\theta\mathrm{c}\psi - \mathrm{c}\phi\mathrm{s}\psi) & -(\mathrm{c}\phi\mathrm{s}\theta\mathrm{c}\psi + \mathrm{s}\phi\mathrm{s}\psi) & 0 & 0 & 0 \\ -\mathrm{c}\theta\mathrm{s}\psi & -(\mathrm{s}\phi\mathrm{s}\theta\mathrm{s}\psi + \mathrm{c}\phi\mathrm{c}\psi) & -(\mathrm{c}\phi\mathrm{s}\theta\mathrm{s}\psi - \mathrm{s}\phi\mathrm{c}\psi) & 0 & 0 & 0 \\ \mathrm{s}\theta & -\mathrm{s}\phi\mathrm{c}\theta & -\mathrm{c}\phi\mathrm{c}\theta & 0 & 0 & 0 \\ 0 & 0 & 0 & -1 & -\mathrm{s}\phi\mathrm{t}\theta & -\mathrm{c}\phi\mathrm{t}\theta \\ 0 & 0 & 0 & 0 & -\mathrm{c}\phi & \mathrm{s}\phi \\ 0 & 0 & 0 & 0 & -\mathrm{s}\phi/\mathrm{c}\theta & -\mathrm{c}\phi/\mathrm{c}\theta \end{bmatrix} \tag{13}$$

For the GS-KM, $\boldsymbol{h}(\boldsymbol{x}) = \boldsymbol{x}$. Therefore, the measurement model of the GS-KM reduces to

$$\boldsymbol{y}_m(t) = \boldsymbol{x}(t) + \boldsymbol{v}(t) \tag{14}$$

This concludes the definition of the GS-KM (given by Eqs. (11)-(14)). To demonstrate the performance of the proposed approach, the AS-KM, used in [25, 26, 15] and given by Eqs. (18) and (20), is also given for comparison. For the sake of explanation, the process model of the AS-KM is briefly shown below. The system variables of the AS-KM are defined as follows [19]:

$$\boldsymbol{x}' = [u_a \; v_a \; w_a \; \phi \; \theta \; \psi]^T \tag{15}$$

$$\boldsymbol{y}'_m = [V_m \; \alpha_m \; \beta_m \; \phi_m \; \theta_m \; \psi_m]^T \tag{16}$$

$$\boldsymbol{v}' = [v_V \; v_\alpha \; v_\beta \; v_\phi \; v_\theta \; v_\psi]^T \tag{17}$$

where u_a, v_a, w_a are the airspeed components expressed in the body-fixed reference frame. V_m, α_m and β_m are the measurements of the true airspeed, angle of attack and angle of sideslip. Other variables, such as $\boldsymbol{u}_m$ and $\boldsymbol{u}^0$, are the same as for the GS-KM.

The AS-KM is given as follows [26]:

$$\begin{cases} \dot{u}_a = (A_{xm} - f_{Ax} - w_{Ax}) + v_a(r_m - f_r - w_r) - w_a(q_m - f_q - w_q) - g\sin\theta \\ \dot{v}_a = (A_{ym} - f_{Ay} - w_{Ay}) - u_a(r_m - f_r - w_r) + w_a(p_m - f_p - w_p) + g\cos\theta\sin\phi \\ \dot{w}_a = (A_{zm} - f_{Az} - w_{Az}) + u_a(q_m - f_q - w_q) - v_a(p_m - f_p - w_p) + g\cos\theta\cos\phi \\ \dot{\phi} = (p_m - f_p - w_p) + (q_m - f_q - w_q)\sin\phi\tan\theta + (r_m - f_r - w_r)\cos\phi\tan\theta \\ \dot{\theta} = (q_m - f_q - w_q)\cos\phi - (r_m - f_r - w_r)\sin\phi \\ \dot{\psi} = (q_m - f_q - w_q)\dfrac{\sin\phi}{\cos\theta} + (r_m - f_r - w_r)\dfrac{\cos\phi}{\cos\theta} \end{cases} \tag{18}$$

By extracting the noise $\boldsymbol{w}$ from the above equations, one can readily obtain $\boldsymbol{f}(\boldsymbol{x}'(t), \boldsymbol{u}_m(t), \boldsymbol{f}^i(t), t)$ and $\mathbf{G}(\boldsymbol{x}'(t))$ and write the equations in the form of Eqs.(1)-(3). The matrix $\mathbf{G}(\boldsymbol{x}'(t))$ is defined as follows:

$$\mathbf{G}(\boldsymbol{x}'(t)) = \begin{bmatrix} -1 & 0 & 0 & 0 & w_a & -v_a \\ 0 & -1 & 0 & -w_a & 0 & u_a \\ 0 & 0 & -1 & v_a & -u_a & 0 \\ 0 & 0 & 0 & -1 & -\sin\phi\tan\theta & -\cos\phi\tan\theta \\ 0 & 0 & 0 & 0 & -\cos\phi & \sin\phi \\ 0 & 0 & 0 & 0 & -\sin\phi/\cos\theta & -\cos\phi/\cos\theta \end{bmatrix} \tag{19}$$

The measurement model is:

$$\boldsymbol{y}'(t) = \boldsymbol{h}(\boldsymbol{x}'(t)) + \boldsymbol{v}'(t), \qquad t = t_i, i = 1, 2, ... \tag{20}$$

where $\boldsymbol{h}(\boldsymbol{x}'(t))$ is the nonlinear output function which can be found in [26].

Remarks: The model used in [19] is a simplified model of the GS-KM used in the present paper. The model used in [19] assumes that the earth is flat and non-rotating, which could introduce errors for long-range flights [27]. In contrast, the GS-KM used in the present paper does not have to assume that the earth is flat and non-rotating.

The advantage of the GS-KM compared to the AS-KM is that the GS-KM can deal with various flight situations and is more robust in the presence of disturbances such as time-varying wind and turbulence, which will be demonstrated in the following sections.

For the GS-KM, the ground speed measurements are assumed to be fault-free while for the AS-KM, the air data measurements are assumed to be fault-free.

2.2. Disturbances and their influence on fault reconstruction

This paper deals with IMU sensor fault reconstruction in the presence of external disturbances. Section 3 considers simulated disturbances while Section 5 deals with real-life disturbances. In this section, the simulated disturbances are presented first. Specifically, two main types of external disturbances are presented: wind shear and turbulence. The speed components of the disturbances in the earth axis and the body axis are denoted by u_w, v_w, w_w and u_w^B, v_w^B, w_w^B respectively. Then, the influence of disturbances on fault reconstruction is analyzed.

2.2.1. Wind shear and turbulence

Wind shear is a rapid change in the wind vector which could be hazardous to aircraft especially when the aircraft is flying at a low altitude [28]. The wind shear model used in this paper is derived from [28] and the wind speed components in the earth frame u_w, v_w and w_w are shown in Fig. 1(a). v_w is assumed to be zero.

Turbulence is a random process which can occur in various flight situations such as in the clouds as well as near mountains [28]. In this paper, the simulated turbulence is generated using the Dryden model. The power spectral density functions of the Dryden turbulence model are given as follows [28]:

$$\Phi_u(\omega_o) = \frac{2\sigma_u^2 L_u}{\pi V} \frac{1}{1 + (L_u \omega_o / V)^2} \tag{21}$$

$$\Phi_v(\omega_o) = \frac{\sigma_v^2 L_v}{\pi V} \frac{1 + 3(L_v \omega_o / V)^2}{1 + (L_v \omega_o / V)^2} \tag{22}$$

$$\Phi_w(\omega_o) = \frac{\sigma_w^2 L_w}{\pi V} \frac{1 + 3(L_w \omega_o / V)^2}{1 + (L_w \omega_o / V)^2} \tag{23}$$

where V is the true airspeed, ω_o is the observed angular frequency. In this paper, the scale lengths $L_u = L_v = L_w = 530$ m, the intensities $\sigma_u = \sigma_v = \sigma_w = 3.54$ m/s. The resulting speed components of the generated turbulence are shown in Fig. 1(b).

2.2.2. Influence of disturbances on fault reconstruction

The influence of the disturbances on fault reconstruction is explained below. It should be noted that the disturbances are included in the modeling of the aircraft response but they are considered unknown when designing fault reconstruction approaches.

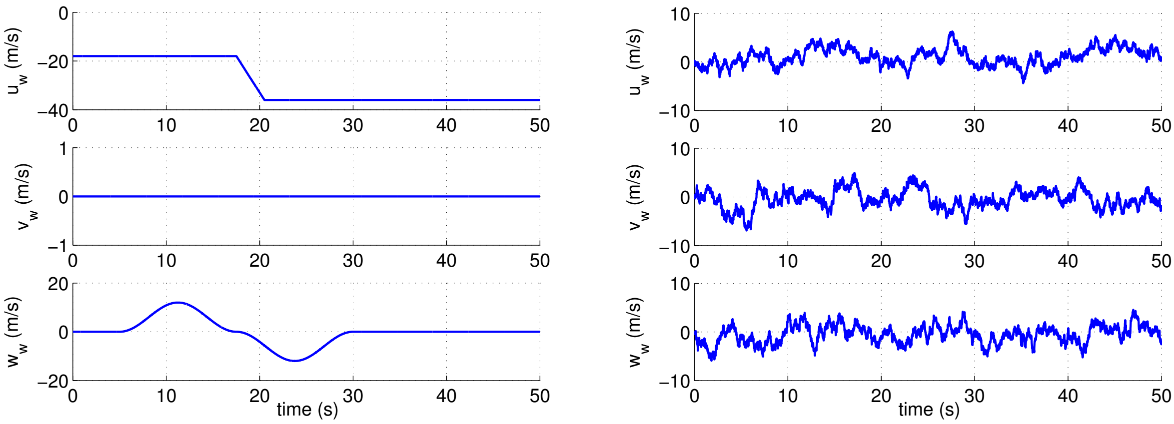

(a) Wind speed components of the simulated wind shear

(b) Wind speed components of the simulated turbulence using the Dryden Model

Figure 1: Two main types of external disturbances: wind shear and turbulence

Define the following:

$$\boldsymbol{V}_a^B = [u_a \ v_a \ w_a]^T, \ \boldsymbol{V}_w^B = [u_w^B \ v_w^B \ w_w^B]^T \tag{24}$$

$$\boldsymbol{A} = [A_x \ A_y \ A_z]^T, \ \boldsymbol{\omega} = [p \ q \ r]^T \tag{25}$$

$$\boldsymbol{f}_A = [f_{Ax} \ f_{Ay} \ f_{Az}]^T, \ \boldsymbol{f}_\omega = [f_p \ f_q \ f_r]^T \tag{26}$$

$$\boldsymbol{w}_A = [w_{Ax} \ w_{Ay} \ w_{Az}]^T, \ \boldsymbol{w}_\omega = [w_p \ w_q \ w_r]^T \tag{27}$$

According to [19], the dynamics of the airspeed can be expressed as

$$\dot{\boldsymbol{V}}_a^B = \boldsymbol{A} + \mathbf{T}_{be}\boldsymbol{g} - \boldsymbol{\omega} \times \boldsymbol{V}_a^B - (\dot{\boldsymbol{V}}_w^B + \boldsymbol{\omega} \times \boldsymbol{V}_w^B) \tag{28}$$

where $\mathbf{T}_{be}$ is the transformation matrix from earth axis to body axis. $\boldsymbol{g} = [0 \ 0 \ g]^T$. Rewrite Eq. (5) and substitute it into Eq. (28), resulting in:

$$\dot{\boldsymbol{V}}_a^B = (\boldsymbol{A}_m - \boldsymbol{f}_A - \boldsymbol{w}_A) + \mathbf{T}_{be}\boldsymbol{g} - (\boldsymbol{\omega}_m - \boldsymbol{f}_\omega - \boldsymbol{w}_\omega) \times \boldsymbol{V}_a^B - (\dot{\boldsymbol{V}}_w^B + (\boldsymbol{\omega}_m - \boldsymbol{f}_\omega - \boldsymbol{w}_\omega) \times \boldsymbol{V}_w^B) \tag{29}$$

Define $\boldsymbol{d}_w = \dot{\boldsymbol{V}}_w^B + (\boldsymbol{\omega}_m - \boldsymbol{f}_\omega - \boldsymbol{w}_\omega) \times \boldsymbol{V}_w^B$. When the wind is constant, $\boldsymbol{d}_w = \mathbf{0}$, the above equation reduces to

$$\dot{\boldsymbol{V}}_a^B = (\boldsymbol{A}_m - \boldsymbol{f}_A - \boldsymbol{w}_\omega) + \mathbf{T}_{be}\boldsymbol{g} - (\boldsymbol{\omega}_m - \boldsymbol{f}_\omega - \boldsymbol{w}_\omega) \times \boldsymbol{V}_a^B \tag{30}$$

which is the vector form of the first three equations of Eq. (18). When the wind is not constant, $\boldsymbol{d}_w \neq \mathbf{0}$. It is seen from Eq. (29) that $\boldsymbol{f}_A$ and $\boldsymbol{d}_w$ have the same distribution matrix ($\mathbf{I}$) and it is difficult to distinguish between them. Consequently, when the AS-KM is used to reconstruct the faults in the presence of external disturbances, the faults and the disturbances are coupled, which could lead to incorrect fault reconstruction.

2.3. Measurements and sensor faults

The aircraft model used in the simulation is the ADMIRE benchmark model [29]. To make the validation more realistic, noise is added to the measurements of the model. This simulation data is used in Section 3 to validate the performance of the proposed approaches while the real flight test data is used in Section 5. The standard deviations of the noises added to the sensors are given in Table 1. In the table, $\sigma_{(\bullet)}$ denotes the standard deviations of the noise in the corresponding sensors.

Table 1: Standard deviations of the noises added in the sensors

Standard deviations	Magnitudes	Units
σ_V	0.1	[m/s]
σ_{U_N}, σ_{U_E}, σ_{U_D}	0.01	[m/s]
σ_α, σ_β	$0.1\pi/180$	[rad]
σ_ϕ, σ_θ, σ_ψ	$0.01\pi/180$	[rad]
σ_{A_x}, σ_{A_y}, σ_{A_z}	0.01	[m/s^2]
σ_p, σ_q, σ_r	$0.01\pi/180$	[rad/s]

In this paper, all the IMU sensors fail simultaneously during 10 s $< t <$ 30 s. This means $\boldsymbol{f}^i = \boldsymbol{0}$ when $t \leq$ 10 s or $t \geq$ 30 s. During 10 s $< t <$ 30 s, the faults $\boldsymbol{f}^i$ are presented in Table 2. As can be seen from the table, different types of faults are considered, including bias faults and drift faults, as well as oscillatory faults. The fault scenario is arbitrarily chosen to test the performance of the proposed approach.

3. IMU sensor fault reconstruction

This section deals with the IMU sensor fault reconstruction problem. First, the newly-developed ATSEKF is introduced in Section 3.1. Then, in Section 3.2, two different strategies are proposed to validate the proposed approach for IMU sensor fault reconstruction. The validation results of the proposed approach

Table 2: Fault information

Time interval	Faults	Fault type	Fault magnitude	Fault unit
10 s $< t <$ 30 s	f_{Ax}	bias	3	[m/s^2]
	f_{Ay}	drift	$0.1(t-10)$	[m/s^2]
	f_{Az}	oscillatory	$4\sin(0.5\pi t)$	[m/s^2]
	f_p	bias	$1.5\pi/180$	[rad/s]
	f_q	oscillatory	$\pi \sin\big(0.5\pi(t-10)\big)/180$	[rad/s]
	f_r	bias	$3\pi/180$	[rad/s]

in the absence of disturbances are shown in Section 3.3. The validation results in the presence of wind shear and turbulence are given in Section 3.4 and 3.5 respectively.

3.1. Adaptive Two-Stage Extended Kalman Filter

In this paper, the ATSEKF is proposed to estimate the states and the faults. The ATSEKF is an improved version of the IOTSEKF [19]. First, the IOTSEKF is introduced. Then, the adaption scheme for the covariance matrix is introduced.

The IOTSEKF is composed of a modified bias-free filter and a bias filter [30, 19]. The bias filter, which estimates the faults, models the faults as: $\boldsymbol{f}_k^i = \boldsymbol{f}_{k-1}^i + \boldsymbol{w}_{k-1}^{\boldsymbol{f}^i}$ with covariances: $E\{\boldsymbol{w}_k^{\boldsymbol{f}^i}(\boldsymbol{w}_l^{\boldsymbol{f}^i})^T\} = \mathbf{Q}_k^{\boldsymbol{f}^i}\delta_{kl}$ and $E\{\boldsymbol{w}_k(\boldsymbol{w}_l^{\boldsymbol{f}^i})^T\} = \mathbf{Q}_k^{\boldsymbol{x}\boldsymbol{f}^i}\delta_{kl}$. $\boldsymbol{w}_k$ is the defined in Eq. (1) and δ_{kl} the Kronecker function. The IOTSEKF, slightly modified from [19] for clarity, is presented below.

1. The bias-free filter of the IOTSEKF is as follows:
   (a) Predicted state and error covariance matrix:

$$\boldsymbol{\eta}_1 = \bar{\boldsymbol{x}}_{k|k-1} = \bar{\boldsymbol{x}}_{k-1|k-1} + \int_{t_{k-1}}^{t_k} \boldsymbol{f}(\bar{\boldsymbol{x}}(t), \boldsymbol{u}_m(t), \mathbf{0}, t)dt + \bar{\boldsymbol{u}}_{k-1} \tag{31}$$

$$\mathbf{P}_{k|k-1}^{\bar{\boldsymbol{x}}} = \boldsymbol{\Phi}_{k-1}\mathbf{P}_{k-1|k-1}^{\bar{\boldsymbol{x}}}\boldsymbol{\Phi}_{k-1}^T + \bar{\mathbf{Q}}_{k-1} \tag{32}$$

   where $\boldsymbol{f}(\bar{\boldsymbol{x}}(t), \boldsymbol{u}_m(t), \mathbf{0}, t)$ means the fault vector is set to $\mathbf{0}$. This is because the IOTSEKF decouples the state and fault estimation. $\bar{\boldsymbol{u}}_{k-1}$ and $\bar{\mathbf{Q}}_{k-1}$ are defined by Eqs. (45) and (46) respectively. Discrete-time matrices $\boldsymbol{\Phi}_{k-1}$ and $\boldsymbol{\Gamma}_{k-1}$ are calculated by:

$$\boldsymbol{\Phi}_{k-1} = e^{\mathbf{F}_{k-1}\Delta t} = \sum_n^{\infty} \frac{\mathbf{F}_{k-1}^n(\Delta t)^n}{n!}, \ \Delta t = t_k - t_{k-1}, \tag{33}$$

$$\mathbf{F}_{k-1} = \left.\frac{\partial \boldsymbol{f}(\boldsymbol{x}(t), \boldsymbol{u}(t), \boldsymbol{f}^i(t))}{\partial \boldsymbol{x}}\right|_{\boldsymbol{x}=\bar{\boldsymbol{x}}_{k-1|k-1}}, \quad \boldsymbol{\Gamma}_{k-1} = \int_{t_{k-1}}^{t_k} \boldsymbol{\Phi}_{k-1}\mathbf{G}(\bar{\boldsymbol{x}}_{k-1|k-1})dt \tag{34}$$

   (b) Kalman gain calculation:

$$\mathbf{H}_k = \frac{\partial \boldsymbol{h}(\boldsymbol{x}(t))}{\partial \boldsymbol{x}}|_{\boldsymbol{x}=\boldsymbol{\eta}_1} \tag{35}$$

$$\mathbf{K}_k^{\bar{\boldsymbol{x}}} = \mathbf{P}_{k|k-1}^{\bar{\boldsymbol{x}}}\mathbf{H}_k^T(\mathbf{H}_k\mathbf{P}_{k|k-1}^{\bar{\boldsymbol{x}}}\mathbf{H}_k^T + \mathbf{R}_k)^{-1} \tag{36}$$

   where $\mathbf{R}_k$ is the covariance matrix defined by $E\{\boldsymbol{v}_k\boldsymbol{v}_l^T\} = \mathbf{R}_k\delta_{kl}$.

   (c) Measurement update:

$$\boldsymbol{\eta}_2 = \bar{\boldsymbol{x}}_{k|k-1} + \mathbf{K}_k^{\bar{\boldsymbol{x}}}\big(\boldsymbol{y}_k - \boldsymbol{h}(\boldsymbol{\eta}_1) - \mathbf{H}_k(\bar{\boldsymbol{x}}_{k|k-1} - \boldsymbol{\eta}_1)\big) \tag{37}$$

   Define $\epsilon := \frac{\|\boldsymbol{\eta}_2 - \boldsymbol{\eta}_1\|}{\|\boldsymbol{\eta}_2\|}$ and ϵ_0 the desired parameter to stop the iteration. If $\epsilon > \epsilon_0$, repeat step (b) and step (c). In this paper, ϵ_0 is chosen to be 10^{-8} and this iteration is only performed in the first ten time steps. After each iteration, $\boldsymbol{\eta}_1 := \boldsymbol{\eta}_2$.

(d) Update the state estimation error covariance matrix, if $\epsilon \leq \epsilon_0$:

$$\bar{\boldsymbol{x}}_{k|k} = \boldsymbol{\eta}_2 \tag{38}$$

$$\mathbf{P}^{\bar{\boldsymbol{x}}}_{k|k} = (\mathbf{I} - \mathbf{K}^{\bar{\boldsymbol{x}}}_k \mathbf{H}_k)\mathbf{P}^{\bar{\boldsymbol{x}}}_{k|k-1}(\mathbf{I} - \mathbf{K}^{\bar{\boldsymbol{x}}}_k \mathbf{H}_k)^T + \mathbf{K}^{\bar{\boldsymbol{x}}}_k \mathbf{R}_k (\mathbf{K}^{\bar{\boldsymbol{x}}}_k)^T \tag{39}$$

2. The bias filter of the IOTSEKF, which is used to estimate the faults, is as follows:

$$\hat{\boldsymbol{f}}^i_{k|k-1} = \hat{\boldsymbol{f}}^i_{k-1|k-1} \tag{40}$$

$$\mathbf{P}^{\boldsymbol{f}^i}_{k|k-1} = \mathbf{P}^{\boldsymbol{f}^i}_{k-1|k-1} + \mathbf{Q}^{\boldsymbol{f}^i}_{k-1} \tag{41}$$

$$\mathbf{K}^{\boldsymbol{f}^i}_k = \mathbf{P}^{\boldsymbol{f}^i}_{k|k-1}\mathbf{S}^T_k(\mathbf{H}_k\mathbf{P}^{\bar{\boldsymbol{x}}}_{k|k-1}\mathbf{H}^T_k + \mathbf{R}_k + \mathbf{S}_k\mathbf{P}^{\boldsymbol{f}^i}_{k|k-1}\mathbf{S}^T_k)^{-1} \tag{42}$$

$$\hat{\boldsymbol{f}}^i_{k|k} = \hat{\boldsymbol{f}}^i_{k|k-1} + \mathbf{K}^{\boldsymbol{f}^i}_k(\boldsymbol{y}_k - \boldsymbol{h}(\bar{\boldsymbol{x}}_{k|k-1}) - \mathbf{S}_k\hat{\boldsymbol{f}}^i_{k|k-1}) \tag{43}$$

$$\mathbf{P}^{\boldsymbol{f}^i}_{k|k} = (\mathbf{I} - \mathbf{K}^{\boldsymbol{f}^i}_k\mathbf{S}_k)\mathbf{P}^{\boldsymbol{f}^i}_{k|k-1} \tag{44}$$

3. The coupling equations of the IOTSEKF are:

$$\bar{\boldsymbol{u}}_{k-1} = (\bar{\mathbf{U}}_k - \mathbf{U}_k)\hat{\boldsymbol{f}}^i_{k-1|k-1} \tag{45}$$

$$\bar{\mathbf{Q}}_{k-1} = \mathbf{\Gamma}_{k-1}\mathbf{Q}_{k-1}\mathbf{\Gamma}^T_{k-1} - \mathbf{Q}^{\boldsymbol{x}\boldsymbol{f}^i}_{k-1}\bar{\mathbf{U}}^T_k - \mathbf{U}_k(\mathbf{Q}^{\boldsymbol{x}\boldsymbol{f}^i}_{k-1} - \bar{\mathbf{U}}_k\mathbf{Q}^{\boldsymbol{f}^i}_{k-1})^T \tag{46}$$

$$\bar{\mathbf{U}}_k = \mathbf{\Phi}_{k-1}\mathbf{V}_{k-1} + \mathbf{\Gamma}_{k-1} \tag{47}$$

$$\mathbf{S}_k = \mathbf{H}_k\mathbf{U}_k \tag{48}$$

where $\mathbf{Q}_{k-1}$ the covariance matrix defined by $E\{\boldsymbol{w}_k\boldsymbol{w}^T_l\} = \mathbf{Q}_k\delta_{kl}$. $\mathbf{U}_k$ and $\mathbf{V}_k$ are the two-stage blending matrices given by

$$\mathbf{U}_k = \bar{\mathbf{U}}_k + (\mathbf{Q}^{\boldsymbol{x}\boldsymbol{f}^i}_{k-1} - \bar{\mathbf{U}}_k\mathbf{Q}^{\boldsymbol{f}^i}_{k-1})(\mathbf{P}^{\boldsymbol{f}^i}_{k|k-1})^{-1} \tag{49}$$

$$\mathbf{V}_k = \mathbf{U}_k - \mathbf{K}^{\bar{\boldsymbol{x}}}_k\mathbf{S}_k \tag{50}$$

4. The final state estimate and its covariance matrix using the IOTSEKF are given as follows:

$$\hat{\boldsymbol{x}}_{k|k} = \bar{\boldsymbol{x}}_{k|k} + \mathbf{V}_k\hat{\boldsymbol{f}}^i_{k|k} \tag{51}$$

$$\mathbf{P}^{\boldsymbol{x}}_{k|k} = \mathbf{P}^{\bar{\boldsymbol{x}}}_{k|k} + \mathbf{V}_k\mathbf{P}^{\boldsymbol{f}^i}_{k|k}\mathbf{V}^T_k \tag{52}$$

The final fault estimation is given in Eq. (43). This concludes the introduction of the IOTSEKF. For the benefit of using the IOTSEKF, please refer to [19] and the reference therein.

Although this IOTSEKF can estimate both the states and faults, its performance can be degraded by bad choices of $\mathbf{Q}^{\boldsymbol{f}^i}_k$ and $\mathbf{Q}^{\boldsymbol{x}\boldsymbol{f}^i}_k$. According to [30], $\mathbf{Q}^{\boldsymbol{x}\boldsymbol{f}^i}_k$ can be chosen to be zero. The present paper proposes an adaptive update scheme for $\mathbf{Q}^{\boldsymbol{f}^i}_k$.

Define $\hat{\mathbf{Q}}_k$ as

$$\hat{\mathbf{Q}}_k := \mathbf{C}_{r,k} - \mathbf{H}_k\mathbf{\Gamma}_{k-1}\mathbf{Q}_{k-1}\mathbf{\Gamma}^T_{k-1}\mathbf{H}^T_k/\Delta t - \mathbf{R}_k \tag{53}$$

where $\mathbf{C}_{r,k} = \frac{1}{N}\sum_{j=k-N+1}^{k} \boldsymbol{\gamma}_j\boldsymbol{\gamma}_j^T$. N is the size of a moving window. In this paper, $N = 10$. $\boldsymbol{\gamma}_j$ is the innovation at time step j which can be calculated by

$$\boldsymbol{\gamma}_j = \boldsymbol{y}_j - \boldsymbol{h}(\boldsymbol{\Phi}_{j-1}\hat{\boldsymbol{x}}_{j-1|j-1} + \boldsymbol{\Gamma}_{j-1}\hat{\boldsymbol{f}}_{j-1|j-1}) \tag{54}$$

In Eq. (53), $\mathbf{Q}_k$ and $\mathbf{R}_k$ are the process noise and measurement noise covariance matrices, which are defined in Eq. (46) and (36) respectively. Take the GS-KM as an example, $\mathbf{R}_k$ can be readily determined by the following

$$\mathbf{R}_k = \mathrm{diag}(\sigma_{U_N}^2, \sigma_{U_E}^2, \sigma_{U_D}^2, \sigma_\phi^2, \sigma_\theta^2, \sigma_\psi^2) \tag{55}$$

where $\sigma_{(\bullet)}$ is given in Table 1. Regarding the process noise covariance matrix $\mathbf{Q}_k$, it should be noted that the input of the KM used by the IOTSEKF is $\boldsymbol{u}_m$. As can be seen from Eq. (1), the only process noise is $\boldsymbol{w}$ which is given in Eq. (7). This is the noise in the IMU sensor measurements. Therefore, $\mathbf{Q}_k$ can be determined by

$$\mathbf{Q}_k = \mathrm{diag}(\sigma_{Ax}^2, \sigma_{Ay}^2, \sigma_{Az}^2, \sigma_p^2, \sigma_q^2, \sigma_r^2) \tag{56}$$

This is also an advantage when using the GS-KM as the model for fault reconstruction since both the process noise and output noise covariance matrices are defined explicitly.

According to covariance matching techniques [31], $\mathbf{Q}_k^{\boldsymbol{f}^i}$ can be updated based on the main diagonal of the following matrix

$$\boldsymbol{\Gamma}_{k-1}^{-1}\mathbf{H}_k^{-1}\tilde{\mathbf{Q}}_k(\mathbf{H}_k^T)^{-1}(\boldsymbol{\Gamma}_{k-1}^T)^{-1}(\Delta t)^2 \tag{57}$$

where $\tilde{\mathbf{Q}}_k$ is determined

$$\tilde{\mathbf{Q}}_k = \mathrm{diag}(\max\{0, \hat{Q}_{11}\}, ..., \max\{0, \hat{Q}_{mm}\}) \tag{58}$$

with $\hat{Q}_{jj}, j = 1, 2, ..., m$ the jth diagonal element of $\hat{\mathbf{Q}}_k$ which is defined in Eq. (53).

The IOTSEKF with this adaption of $\mathbf{Q}_k^{\boldsymbol{f}^i}$ is called ATSEKF. In the following of this paper, this ATSEKF is used as the filter for both state and fault reconstruction.

3.2. Closed-loop validation vs open-loop validation

In this section, two different validation strategies are presented. The aircraft model used in this section is the ADMIRE benchmark model [29]. The controller is the baseline controller of the benchmark model. It contains a longitudinal controller which controls the airspeed, pitch rate and load factor, and a lateral controller which controls the roll rate and angle of sideslip [29]. The controller design is based on the PID control law. More detailed information can be found in [29].

The first validation strategy is the closed-loop validation which is shown in Fig. 2(a). This is the strategy to achieve Fault-Tolerant Control (FTC) in the presence of sensor faults. As can be seen from the figure, after the occurrence of the sensor faults, a fault reconstruction block is implemented to compensate for the sensor faults.

Let $\boldsymbol{u}_m^0$ denote the IMU sensor measurements without faults, then

$$\boldsymbol{u}_m^0 = \boldsymbol{u}^0 + \boldsymbol{w} = \boldsymbol{u}_m - \boldsymbol{f}^i \tag{59}$$

where $\boldsymbol{u}_m$, $\boldsymbol{u}^0$, $\boldsymbol{w}$ and $\boldsymbol{f}^i$ are defined in Eqs. (5), (6), (7) and (8) respectively. Let subscript 'CL' denote the corresponding variables in the closed-loop validation. The fault reconstruction block receives the measurements $\boldsymbol{y}_{m,CL}$ and $\boldsymbol{u}_{m,CL}$, and output unbiased estimates of the state $\boldsymbol{x}_{CL}$ and the faults $\boldsymbol{f}_{CL}^i$ online by making use of the ATSEKF. Without this fault reconstruction block, the estimate of $\boldsymbol{x}_{CL}$ will be biased due to the faults in the sensors.

Since $\boldsymbol{f}_{CL}^i$ are also estimated in an unbiased sense by using the ATSEKF, a more reliable IMU measurement can be obtained by

$$\hat{\boldsymbol{u}}_{m,CL} = \boldsymbol{u}_{m,CL} - \hat{\boldsymbol{f}}_{CL}^i \tag{60}$$

where $\hat{\boldsymbol{u}}_{m,CL}$ denotes the estimated IMU measurements. Due to this fault reconstruction, FTC can be achieved in the presence of faults by making use of $\hat{\boldsymbol{x}}_{CL}$ and $\hat{\boldsymbol{u}}_{m,CL}$. The estimated faults $\hat{\boldsymbol{f}}_{CL}^i$ can also be used for fault detection.

Although the sensor FTC (closed-loop validation) can be validated in simulation, it is difficult to be validated in real-life especially for fixed-wing manned aircraft. For these aircraft, validation with fault injection during the flight is risky. Consequently, this prevents researchers from validating fault reconstruction approaches under real-life uncertainties and disturbances.

In this research, an alternative validation strategy (open-loop validation strategy) is implemented and compared to the closed-loop validation. The open-loop validation strategy is shown in Fig. 2(b) where the subscript 'OL' denotes the corresponding variables in the open-loop validation. It is seen from the figure that only the blocks within the blue dashed line are run online or on-board, and they are free from the influence of the sensor faults. The fault injection and reconstruction are not in the feedback loop. Specifically, the faults are injected into the recorded measurements and are estimated by the fault reconstruction block off-line. In the figure, $\hat{\boldsymbol{x}}_{OL}^a$ and $\hat{\boldsymbol{u}}_{m,OL}^a$, which are the estimated $\boldsymbol{x}_{OL}$ and $\boldsymbol{u}_{m,OL}$ by the Filter block on-board the aircraft, are assumed to be unbiased.

Comparing these two validation strategies, it can be inferred that if the estimates $\hat{\boldsymbol{x}}$ and $\hat{\boldsymbol{f}}^i$ in the closed-loop and the open-loop are unbiased, then the differences between these two strategies are limited. Note that unbiased $\hat{\boldsymbol{f}}^i$ indicates unbiased $\hat{\boldsymbol{u}}_m$. In the following section, the comparison between these two strategies will be shown.

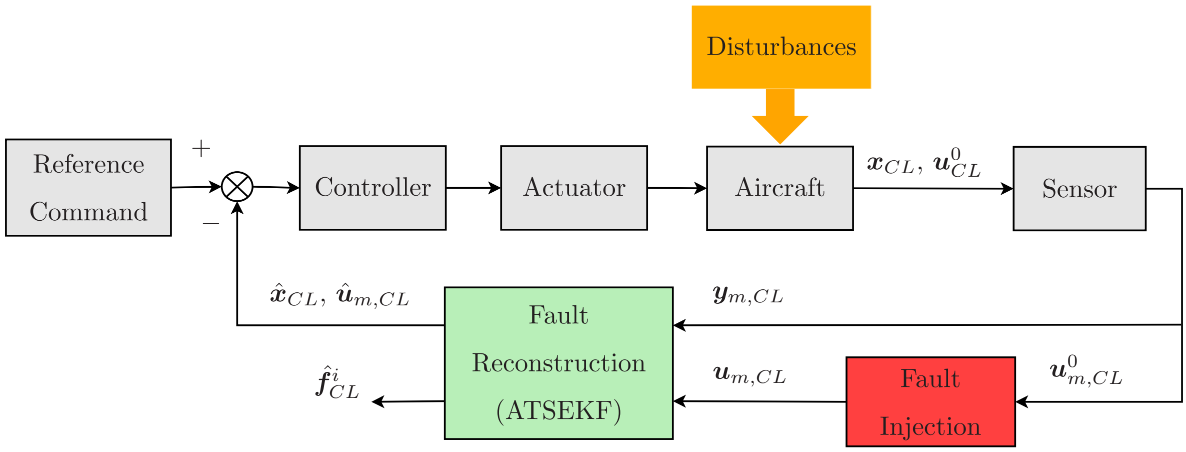

(a) Closed-loop validation strategy (Sensor FTC strategy). The states which are irrelevant to the fault reconstruction are not shown in the figure. All the blocks are run online including the fault injection and fault reconstruction. The subscript 'CL' denotes closed-loop validation.

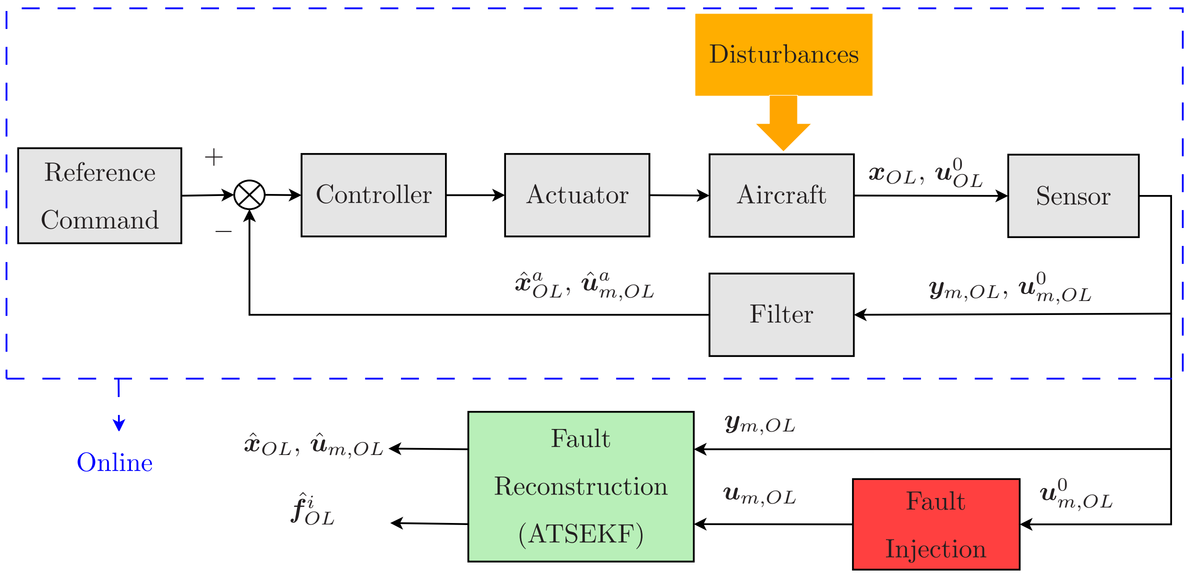

(b) Open-loop validation strategy. The states which are irrelevant to the fault reconstruction are not shown in the figure. The blocks within the blue dashed line are run online while the fault injection and reconstruction are run off-line and are not in the feedback loop. The subscript 'OL' denotes open-loop validation.

Figure 2: Block diagram of two different validation strategies

3.3. Simulation validation in the absence of simulated disturbances

In this section, the results of the above-mentioned two validation strategies are shown. The fault scenario is shown in Table 2. No disturbance is present. The model used is the GS-KM.

The differences of the true states ($\boldsymbol{x} = [U_N, U_E, U_D, \phi, \theta, \psi]^T$) between the open-loop ($\boldsymbol{x}_{OL}$) and closed-loop ($\boldsymbol{x}_{CL}$) validations are shown in Fig. 3(a) and Fig. 3(b). It should be noted that for the closed-loop

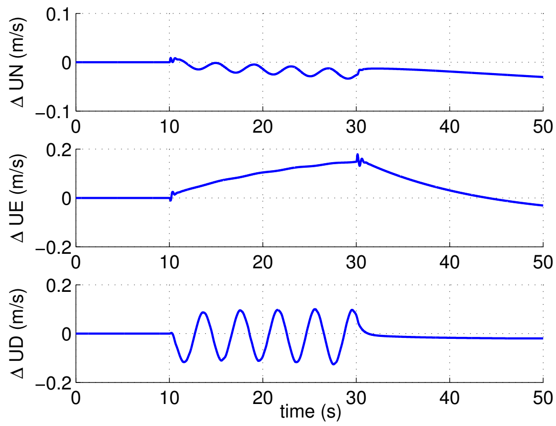

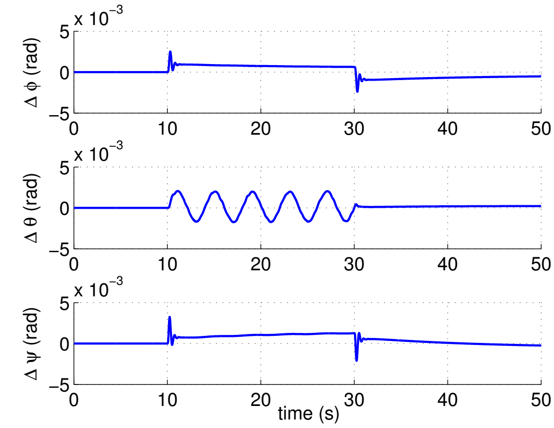

(a) Difference of the true U_N, U_E and U_D between the closed-loop and open-loop validations

(b) Difference of the true ϕ, θ and ψ between the closed-loop and open loop validations

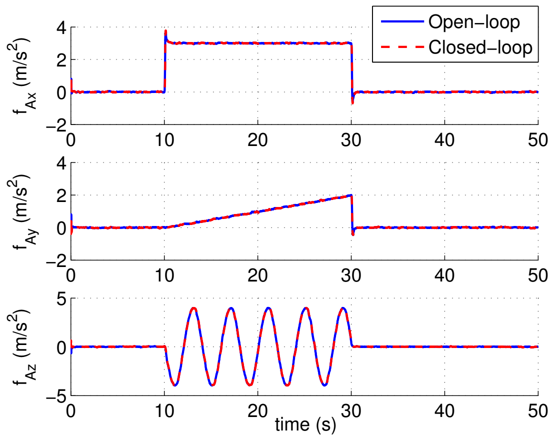

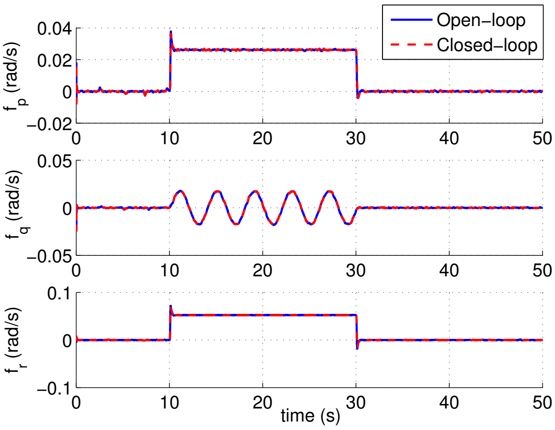

(c) Estimated f_{Ax}, f_{Ay} and f_{Az} of the closed-loop and open-loop validations

(d) Estimated f_p, f_q and f_r of the closed-loop and open-loop validations

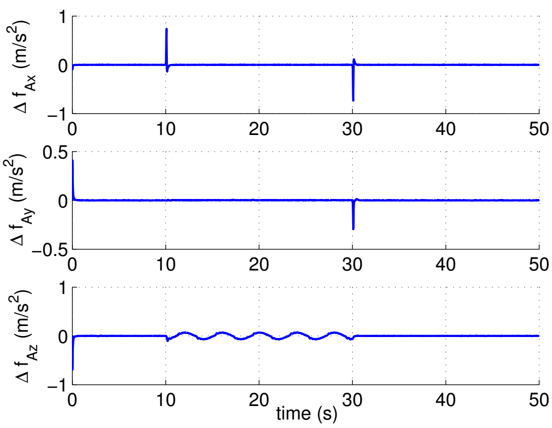

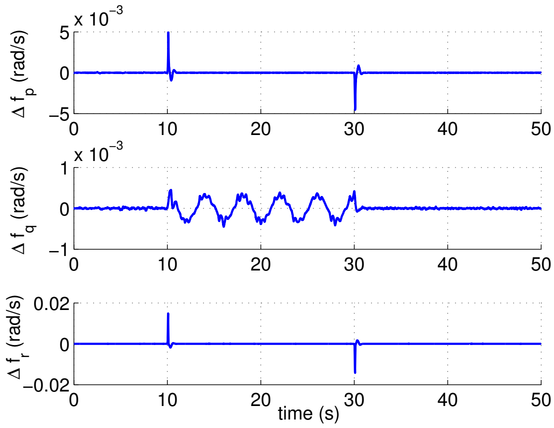

(e) Difference of the estimated f_{Ax}, f_{Ay} and f_{Az} between the closed-loop and open-loop validations

(f) Difference of the estimated f_p, f_q and f_r between the closed-loop and open-loop validations

Figure 3: Comparisons between the open-loop and closed-loop validations in the absence of disturbances

validation, the faults are generated online in the feedback loop. As can be seen from the figure, although the faults are in the feedback loop of closed-loop validation, the differences between $\boldsymbol{x}_{OL}$ and $\boldsymbol{x}_{CL}$ are limited even in the presence of faults. The maximum difference of U_N, U_E and U_D is smaller than 0.2 m/s and that of ϕ, θ and ψ is smaller than 5×10^{-3} rad.

The fault reconstruction results of the two validations are shown in Fig. 3(c) and 3(d). As can be seen, the fault estimates $\hat{\boldsymbol{f}}^i$ ($\hat{f}_{Ax}$, $\hat{f}_{Ay}$, $\hat{f}_{Az}$ and $\hat{f}_p$, $\hat{f}_q$, $\hat{f}_r$) of the two validation strategies, denoted by $\hat{\boldsymbol{f}}^i_{OL}$ and $\hat{\boldsymbol{f}}^i_{CL}$ in the open-loop and closed-loop validations respectively, closely match each other. This indicates that reconstructed faults are similar no matter whether it is the open-loop or closed-loop validation. The state estimates of the open-loop and closed-loop validations, denoted by $\hat{\boldsymbol{x}}_{OL}$ and $\hat{\boldsymbol{x}}_{CL}$ respectively, are both unbiased. The differences between $\hat{\boldsymbol{x}}_{OL}$ and $\hat{\boldsymbol{x}}_{CL}$ are similar to those shown in Fig. 3(a) and Fig. 3(b) and are not shown.

Let us further check the differences between $\hat{\boldsymbol{f}}^i_{OL}$ and $\hat{\boldsymbol{f}}^i_{CL}$ which are shown in Fig. 3(e) and 3(f). It can be seen that the differences mainly occur in the beginning or the end of the fault period (except for $\hat{f}_{Az}$ and $\hat{f}_q$ which are oscillatory faults). During 10 s$< t <$ 30 s, although the true states of the two validations ($\boldsymbol{x}_{OL}$ and $\boldsymbol{x}_{CL}$) are different (as shown in Fig. 3(a) and Fig. 3(b)), the differences between $\hat{\boldsymbol{f}}^i_{OL}$ and $\hat{\boldsymbol{f}}^i_{CL}$ are limited. This becomes more obvious when the faults are removed after $t > 30$ s. $\boldsymbol{x}_{OL}$ and $\boldsymbol{x}_{CL}$ are different (see Fig. 3(a) and Fig. 3(b)), but $\hat{\boldsymbol{f}}^i_{OL}$ and $\hat{\boldsymbol{f}}^i_{CL}$ are all zero-mean.

The above results demonstrate that if the fault reconstruction block can provide unbiased estimates of $\boldsymbol{x}$ and $\boldsymbol{f}^i$, the differences between the two validation strategies are limited. Under this condition, the open-loop validation, which injects and estimates the faults offline, is also valid. Therefore, open-loop validation can be used to test the performance of fault reconstruction approaches under real-life disturbances and uncertainties, as will be shown in Section 5.

In the following sections, the subscript 'OL' and 'CL' will be dropped for readability. In the remainder of this section, all the results are obtained using the closed-loop validation while in Section 5, all the results are obtained using the open-loop validation.

3.4. Simulation validation in the presence of simulated wind shear

In this section, the simulated wind shear, as shown in Fig. 1(a), is included in the simulation model but is assumed unknown for the design of the fault reconstruction approaches. The GS-KM together with the ATSEKF are used for the fault reconstruction. The AS-KM together with the ATSEKF are also used for comparison.

The fault reconstructions of f_{Ax}, f_{Ay} and f_{Az} using the AS-KM and the GS-KM are compared in Fig. 4(a). It is seen that the fault estimates using the GS-KM can follow the true faults well. The fault estimation using the AS-KM is not satisfactory. Estimation of f_{Az} significantly deviates from the true faults around $t = 5$ s. This is caused by the fact the $w_w > 0$ after $t = 5$ s. The vertical wind is interpreted into a

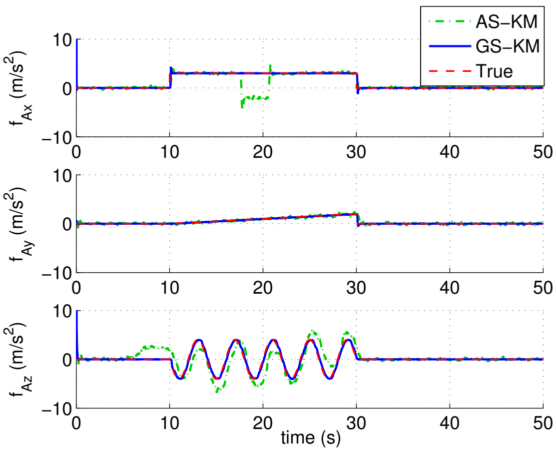

(a) True and estimated f_{Ax}, f_{Ay} and f_{Az} using the AS-KM and GS-KM

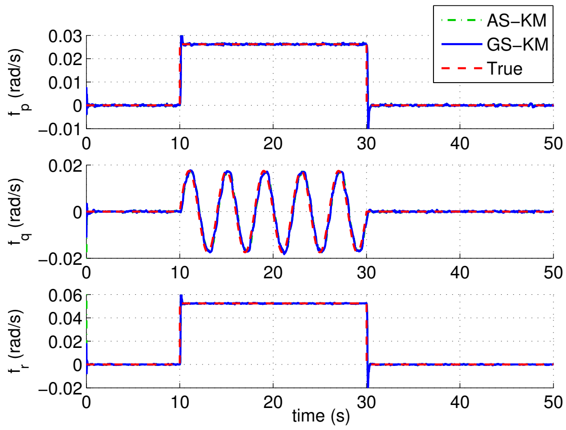

(b) True and estimated f_p, f_q and f_r using the AS-KM and GS-KM

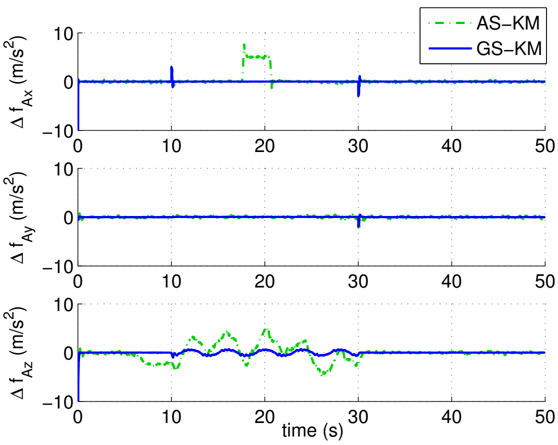

(c) Estimation errors of f_{Ax}, f_{Ay} and f_{Az} using the AS-KM and GS-KM

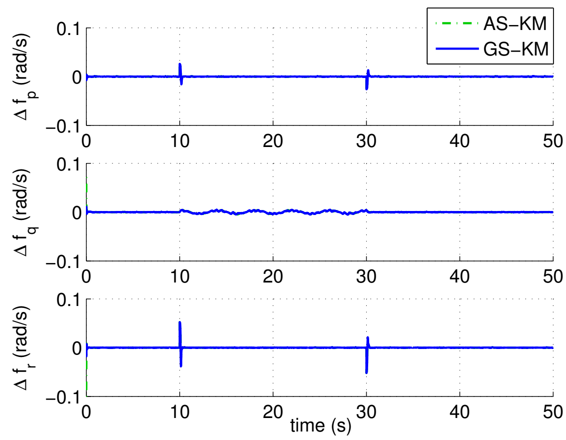

(d) Estimation errors of f_p, f_q and f_r using the AS-KM and GS-KM

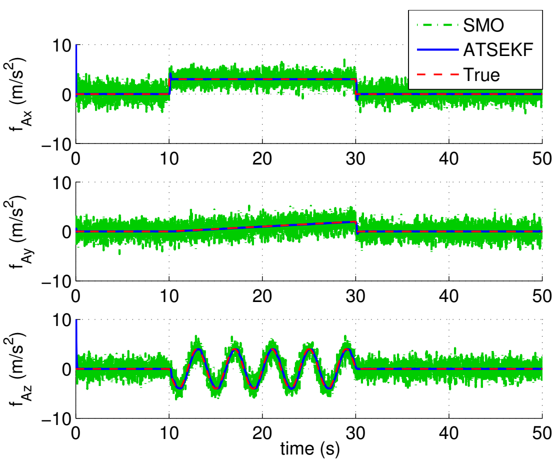

(e) True and estimated f_{Ax}, f_{Ay} and f_{Az} using the SMO and the ATSEKF together with the GS-KM

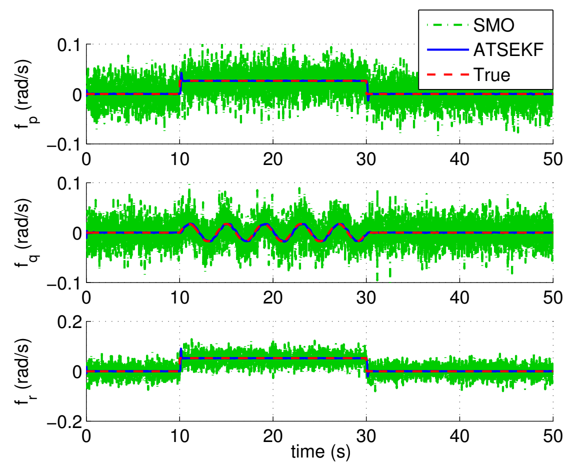

(f) True and estimated f_p, f_q and f_r using the SMO and the ATSEKF together with the GS-KM

Figure 4: State estimation and fault estimation results in the presence of simulated wind shear

fault in the sensor which measures a_z. The reason can be explained using Eq. (29). When w_w is not constant, f_{Az} is coupled with the influence of the wind which leads to the wrong fault reconstruction. Similarly, the estimation of f_{Ax} using the AS-KM between 18 s $< t <$ 20 s is wrong due to u_w which significantly decreases during 18 s $< t <$ 20 s, as shown in Fig. 1(a). Since v_w is assumed to be zero, estimation of f_{Ay} is not influenced. The estimates of f_p, f_q and f_r using the AS-KM and GS-KM are similar and are shown in Fig. 4(b).

The corresponding estimation errors of f_{Ax}, f_{Ay} and f_{Az} using the AS-KM and the GS-KM are shown in Fig. 4(c). As can be seen, the errors using the GS-KM maintain zero-mean while those using the AS-KM deviate from zero. The estimation errors of f_p, f_q and f_r using the two KMs are similar and zero-mean, as shown in Fig. 4(d).

To demonstrate the performance of the ATSEKF, a SMO [32, 33] is implemented using the GS-KM. The estimation of f_{Ax}, f_{Ay}, f_{Az} and f_p, f_q, f_r using the SMO are shown in Fig. 4(e) and 4(f) respectively. As can be seen from the figure, although the faults are reconstructed, the standard deviations of the estimation are significantly larger than those of the ATSEKF. This is caused by the noise in the measurements. The influence of the noise on the fault reconstruction can be reduced by using a low-pass filter, which will be discussed in the following section.

3.5. Simulation validation in the presence of simulated turbulence

In this section, the simulated turbulence, as shown in Fig. 1(b), is included in the simulation but is considered unknown for the design of the fault reconstruction approaches. The GS-KM is again compared with the AS-KM.

If the AS-KM is used when the turbulence is present, as can be seen from Eq. (29), f_{Ax}, f_{Ay} and f_{Az} are coupled with the influence of the turbulence, denoted by $\boldsymbol{d}_w$. This explains why the estimates of f_{Ax}, f_{Ay} and f_{Az} using the AS-KM are corrupted by the turbulence, as shown in Fig. 5(a). Using the GS-KM, satisfactory fault estimation results are achieved, as shown in Fig. 5(a).

The estimates of f_p, f_q and f_r using the two KMs are satisfactory and are the same as in Fig. 4(b). The estimation errors of f_p, f_q and f_r using the two KMs are the same as in Fig. 4(d) and are not shown.

To show the performance of the ATSEKF, the SMO is implemented again to estimate the faults using the GS-KM. Since the standard deviations of the fault estimation are large, a low-pass filter is implemented to filter the estimated faults and the results are shown in Fig. 5(c) and 5(d) respectively. Although the estimates of the SMO are filtered, the standard deviations are still larger than those of the ATSEKF. Therefore, in the following sections, only the results using the ATSEKF are presented.

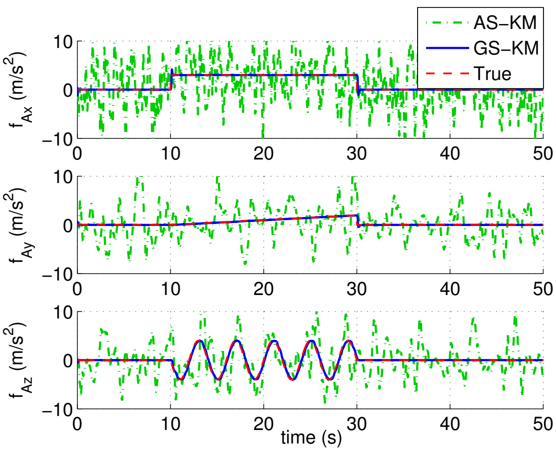

(a) True and estimated f_{Ax}, f_{Ay} and f_{Az} using the AS-KM and GS-KM

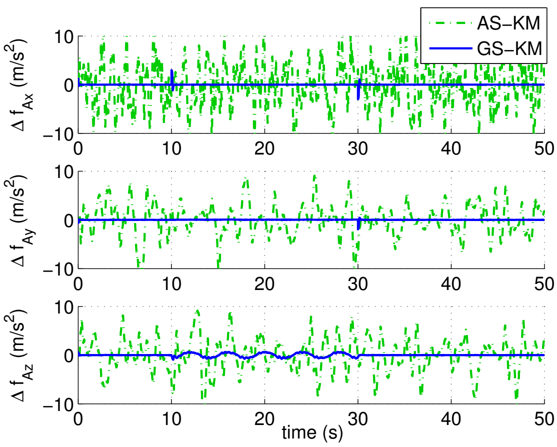

(b) Errors of estimates of f_{Ax}, f_{Ay} and f_{Az} using the AS-KM and GS-KM

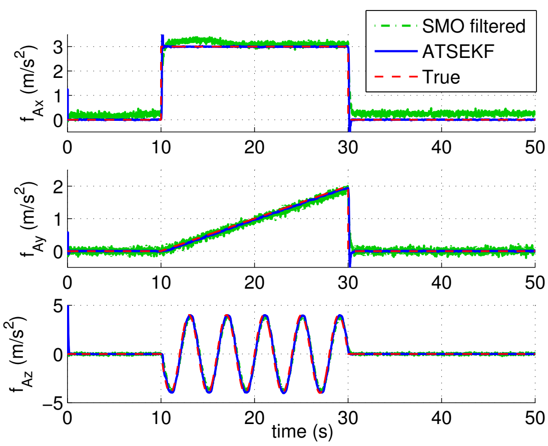

(c) True and estimated f_{Ax}, f_{Ay} and f_{Az} using the SMO and the ATSEKF together with the GS-KM

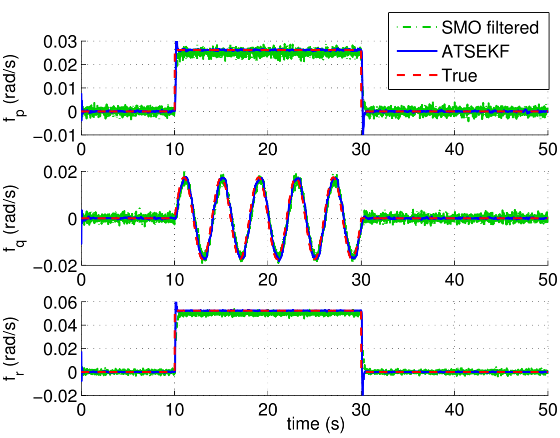

(d) True and estimated f_p, f_q and f_r using the SMO (filtered) and the ATSEKF together with the GS-KM

Figure 5: State estimation and fault estimation results in the presence of simulated turbulence

Figure 6: Cessna Citation II aircraft, owned by Delft University of Technology and the Dutch Aerospace Laboratory

4. Real flight test scenarios

The above results are obtained using a simulated aircraft model. However, to fully demonstrate the performance of the proposed approach, it should be validated using real flight data where realistic uncertainties and disturbances are included. The robustness of the approach should be validated using different flight conditions and wind conditions. In Lu et al. [19], real flight data is also used to validate the performance. However, no turbulence is present in the flight data. Consequently, the robustness of the proposed approach in the presence of disturbances such as time-varying wind and turbulence is not validated.

In order to validate the performance of the proposed approach in the presence of disturbances, more flight tests were performed in 2015. The aircraft used is the Cessna Citation II aircraft which is shown in Fig. 6. Aircraft response data are recorded in various flight conditions and wind conditions. Parabolic flights or so called zero-g flights, during which the aircraft follows a parabolic trajectory to achieve a temporary sensation of weightlessness, are performed in order to test the performance of the approach over a wide range of the flight envelope with varying uncertainties. The measurement data were recorded for post-flight analysis.

The air data are measured with a frequency of 100 Hz and the angle of attack is measured by a mechanical vane on the fuselage used for stall warning. This is different from the measurements used in the flight tests in [19] where the angle of attack is measured by the vanes mounted on an air data boom. The ground speed components are measured by a Global Positioning System receiver at 1 Hz and are linearly interpolated to obtain data with a frequency of 100 Hz. Aircraft response data in the presence of turbulence are also recorded and the crew recorded the time when the turbulence occurs.

In this paper, three representative flight scenarios are chosen to validate the performance of the proposed approach and to show the advantage of the proposed approach over other methods. The three flight scenarios are shown in Fig. 7 and the descriptions are as follows:

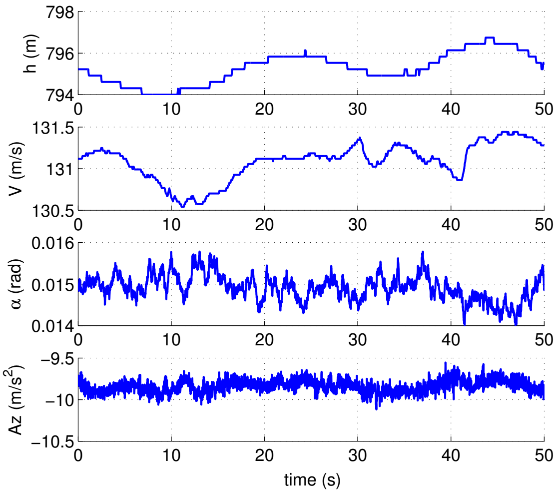

(a) Aircraft response data during the level flight

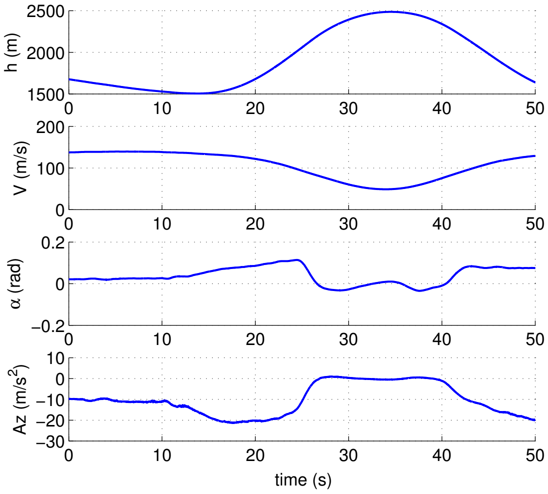

(b) Aircraft response data during the parabolic flight

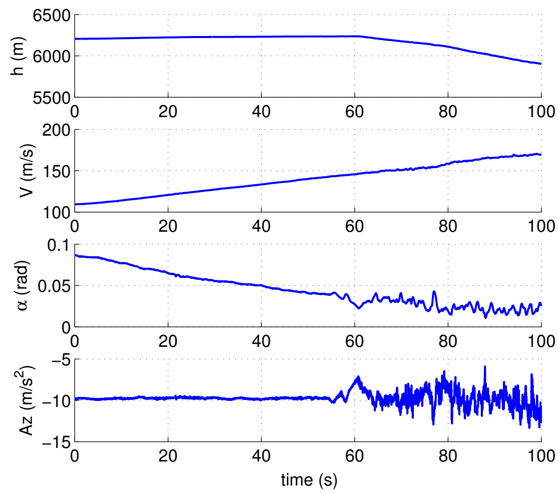

(c) Aircraft response data in the presence of turbulence, only the data between 50 s $< t <$ 100 s are used in the sensor fault reconstruction validation

Figure 7: Real flight test data in different flight scenarios

1. Scenario 1 is a level flight which is shown in Fig. 7(a). As can be seen, the altitude of the aircraft h is nearly constant and so are other parameters such as the true airspeed V, angle of attack α and specific force A_z. In this flight scenario, no manoeuvre is performed which means that there is no controlled excitation.
2. Scenario 2 is a parabolic flight which is shown in Fig. 7(b). As can be seen from the figure, A_z of the aircraft decreases to almost -20 m/s^2 at around $t = 16$ s and increases to almost 0 m/s^2 at around $t = 27$ s. This clearly shows the motion of the aircraft. During this period, the altitude h, true airspeed V and angle of attack α of the aircraft change significantly. At around $t = 28$ s, α even decreases below 0 rad. This scenario is to test the performance over a wide range of the flight envelope.
3. Scenario 3 is a flight in the presence of turbulence which is shown in Fig. 7(c). In the first 60 s, A_z is smooth while after $t = 60$ s, it oscillates significantly. The oscillations are also observable in α. This scenario is to test the performance of the fault reconstruction approaches in the presence of turbulence. In the validation, only the data between 50 s $< t <$ 100 s are used.

In the following section, the performance of the GS-KM will be compared to the AS-KM using these three flight scenarios.

5. Validation using real flight data under various flight scenarios

In this section, the performance of the proposed approach is validated using the flight scenarios in the previous section. Since injecting faults during flight is unfeasible due to safety concerns, this section uses the open-loop validation strategy to validate the fault reconstruction approaches. As shown in Section 3, this is also an effective validation strategy if the states and faults are estimated in an unbiased sense. All the faults are injected into the recorded data and the fault scenario is the same as in Table 2. The filter used for the estimation of the states and faults is the ATSEKF. The performance of the proposed approach as well as the comparison with the approach using the AS-KM are presented in the following.

5.1. Validation of real flight test scenario 1

In this section, the performance of the fault reconstruction of flight scenario 1 is presented. The state estimation performance of the GS-KM is shown in Fig. 8(a) and 8(b). In the figure, the measured states are plotted since real states are not available. As can be seen, the estimated states closely match the measured states. The differences between the measured and estimated states are shown in Fig. 8(c) and 8(d). It can be seen that even during the period when there are faults, the differences between the measured and estimated states are small. This demonstrates that the ATSEKF can provide unbiased state estimates even in the presence of faults.

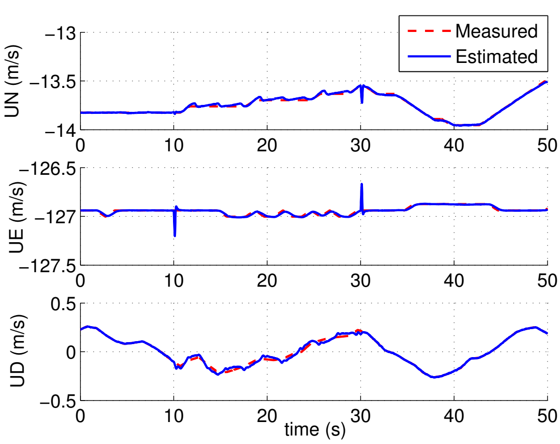

(a) Measured and estimated U_N, U_E and U_D using the GS-KM

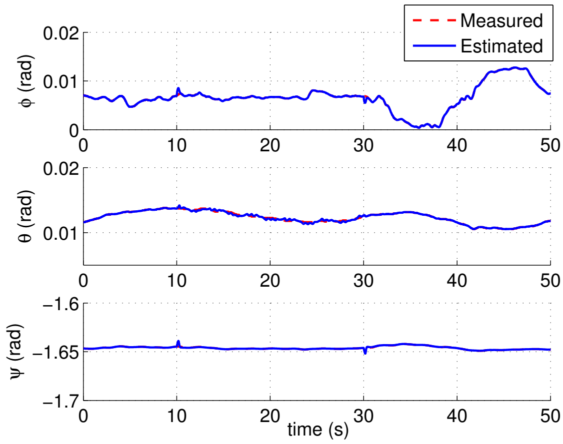

(b) Measured and estimated ϕ, θ and ψ using the GS-KM

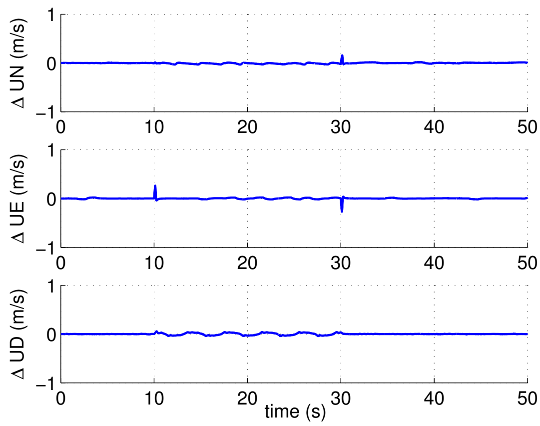

(c) Difference between measured and estimated U_N, U_E and U_D using the GS-KM

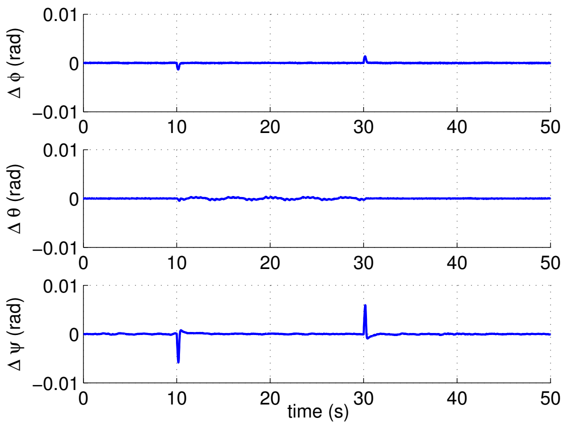

(d) Difference between measured and estimated ϕ, θ and ψ using the GS-KM

Figure 8: State estimation results of real flight test scenario 1

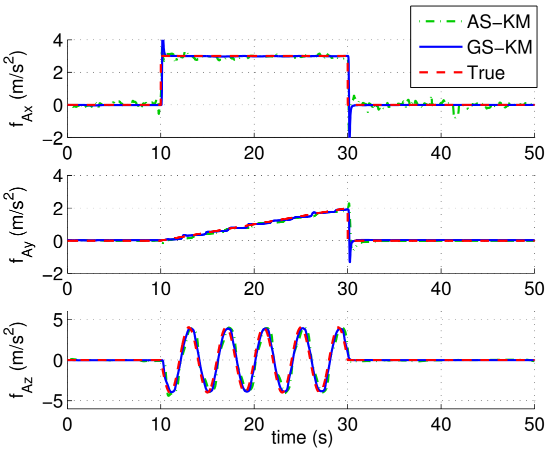

(a) True and estimated f_{Ax}, f_{Ay} and f_{Az} using the AS-KM and GS-KM

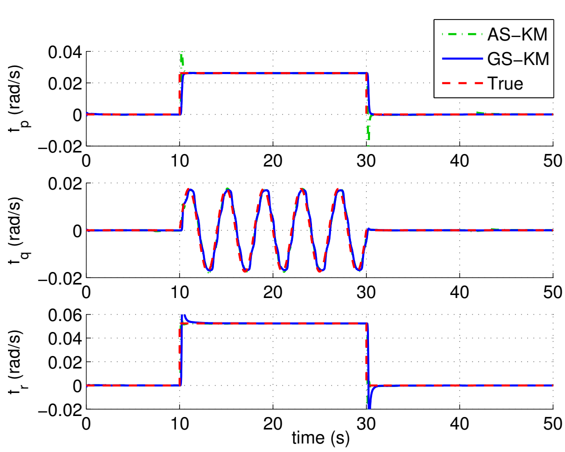

(b) True and estimated f_p, f_q and f_r using the AS-KM and GS-KM

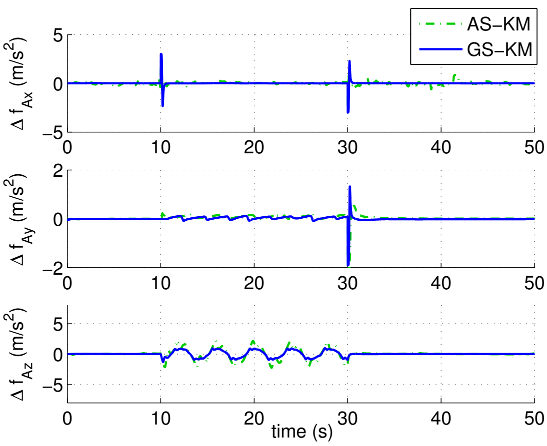

(c) Errors of estimates of f_{Ax}, f_{Ay} and f_{Az} using the AS-KM and GS-KM

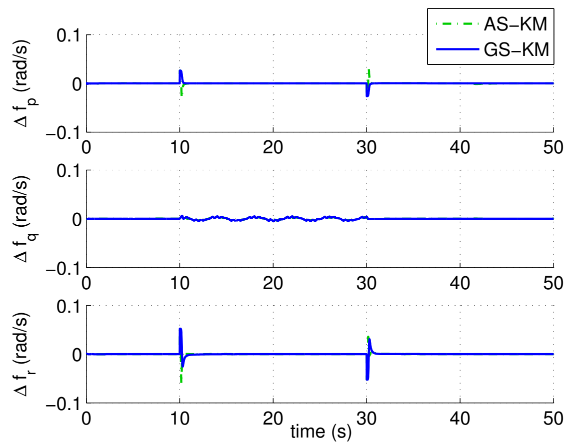

(d) Errors of estimates of f_p, f_q and f_r using the AS-KM and GS-KM

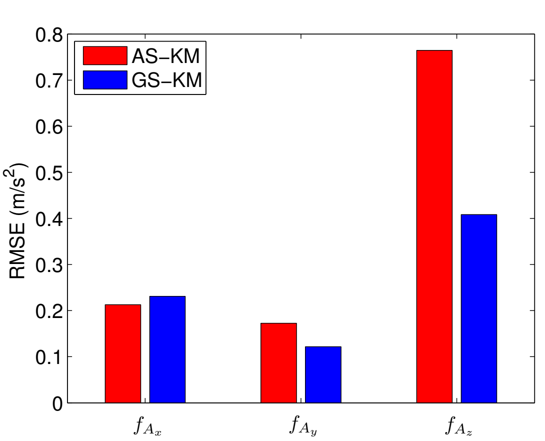

(e) RMSEs of the estimates of f_{Ax}, f_{Ay} and f_{Az}

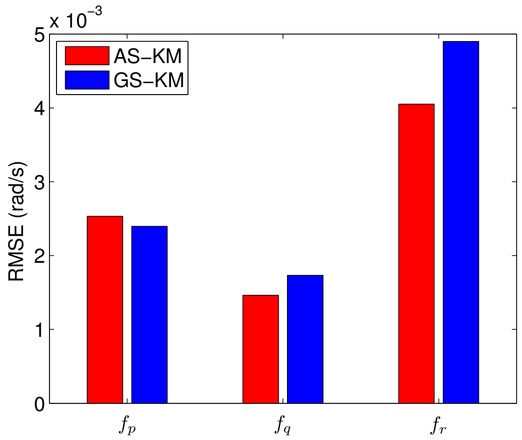

(f) RMSEs of the estimates of f_p, f_q and f_r

Figure 9: Fault estimation results of real flight test scenario 1 (level flight)

The fault estimates using the AS-KM and GS-KM are compared in Fig. 9(a) and 9(b). The true injected faults are also plotted to show the performance of the fault reconstruction. It can be seen from the figure that the performances of using the GS-KM and the AS-KM are comparable. Both of the estimates follow the true faults well.

The estimation errors of f_{Ax}, f_{Ay} and f_{Az} using the two KMs are shown in Fig. 9(c) while those of f_p, f_q and f_r are given in Fig. 9(d). It is seen that the estimation errors using the two KMs are both zero-mean. The estimation error of f_{Az} using the AS-KM is slightly larger than that using the GS-KM in the presence of faults, as can be seen from Fig. 9(c).

The RMSEs of the fault estimates using the two KMs are compared in Fig. 9(e) and 9(f). The RMSEs of the estimates using the two approaches are comparable except for f_{Az}. For the RMSE of the estimate of f_{Az}, the result using the AS-KM is almost twice the result using the GS-KM.

In this flight scenario, the performance using the two KMs is similar. According to Eq. (28), it can be inferred that the wind during this level flight is close to constant.

5.2. Validation of real flight test scenario 2

In this flight scenario, the aircraft is performing a parabolic flight. As can be seen from the measured states shown in Fig. 7(b). All the states change significantly especially during 16 s $< t <$ 26 s and 40 s $< t <$ 50 s. Therefore, it can test the performance over a wide range of the flight envelope.

The estimates of f_{Ax}, f_{Ay} and f_{Az} using the AS-KM and GS-KM are compared in Fig. 10(a). The results using the AS-KM are worse than those using the GS-KM. It is noticed that during 16 s $< t <$ 26 s and 40 s $< t <$ 50 s, the performances using the two KMs both degrade. This is caused by the fact that the system states are changing significantly. However, the performance using the GS-KM is better than that using the AS-KM. The estimates of f_{Ax} using the AS-KM deviate from the true fault condition even at the beginning of the simulation. In contrast, the estimates using the GS-KM maintain zero-mean before the injection of the faults. The estimation errors of f_{Ax}, f_{Ay} and f_{Az} using the AS-KM and GS-KM are compared in Fig. 10(c)

The estimates of f_p, f_q and f_r using the two KMs are similar, as shown in Fig. 10(b). The corresponding errors of the estimation are shown in Fig. 10(d). It is seen that the estimation performance is satisfactory. The maximum error is less than 0.05 rad/s even when the faults are injected.

The RMSEs of the fault estimates using the two KMs are shown in Fig. 10(e) and 10(f), which confirms the better performance of using the GS-KM over the AS-KM.

5.3. Validation of real flight test scenario 3

In this flight scenario, the aircraft is flying in turbulence. The estimates of f_{Ax}, f_{Ay} and f_{Az} using the two KMs are compared in Fig. 11(a). The influence of turbulence on fault reconstruction when using the

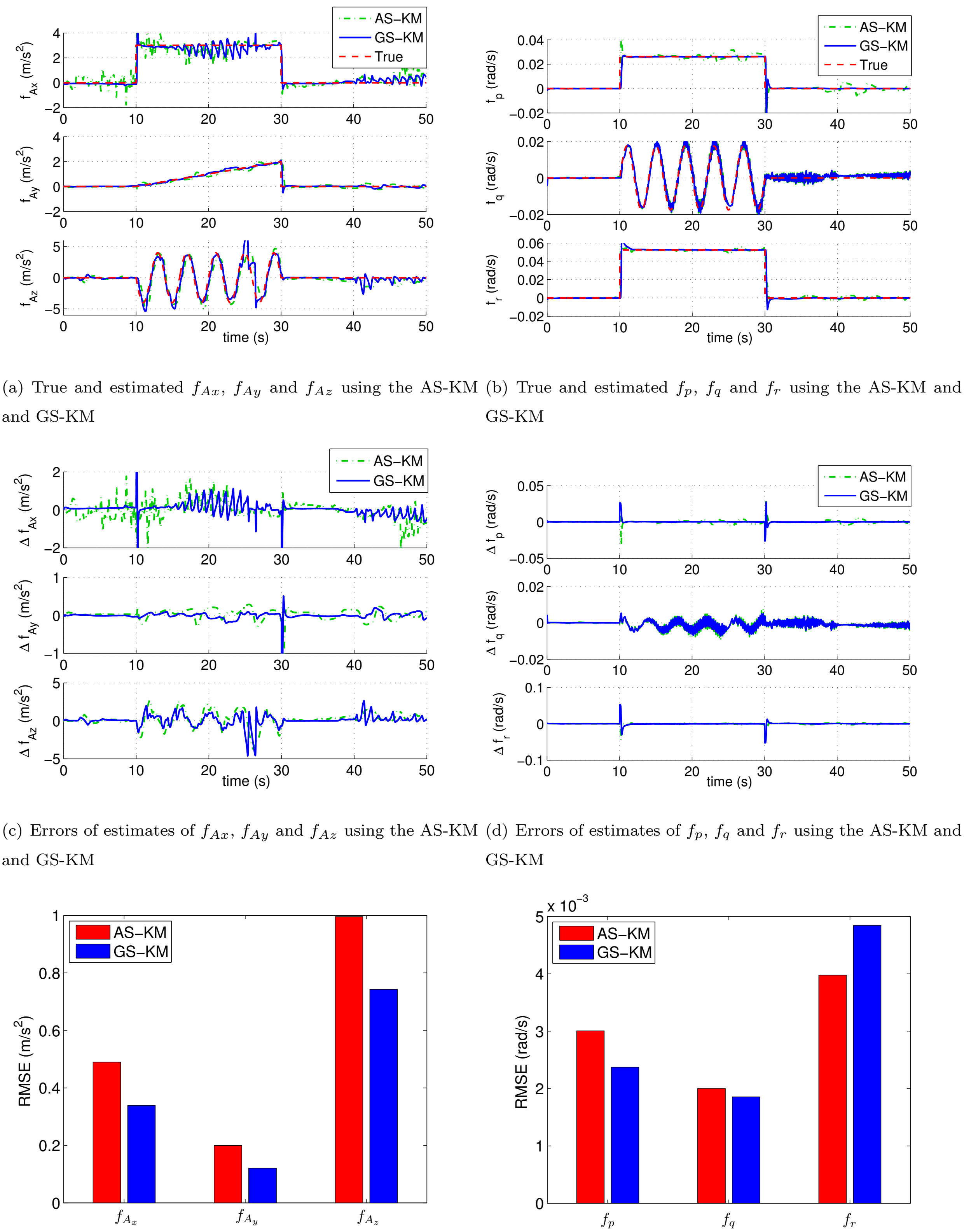

(a) True and estimated f_{Ax}, f_{Ay} and f_{Az} using the AS-KM and GS-KM

(b) True and estimated f_p, f_q and f_r using the AS-KM and GS-KM

(c) Errors of estimates of f_{Ax}, f_{Ay} and f_{Az} using the AS-KM and GS-KM

(d) Errors of estimates of f_p, f_q and f_r using the AS-KM and GS-KM

(e) RMSEs of the estimates of f_{Ax}, f_{Ay} and f_{Az}

(f) RMSEs of the estimates of f_p, f_q and f_r

Figure 10: Fault estimation results of real flight test scenario 2 (parabolic flight)

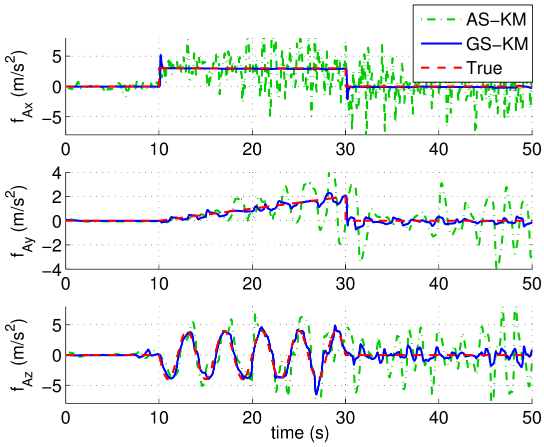

(a) True and estimated f_{Ax}, f_{Ay} and f_{Az} using the AS-KM and GS-KM

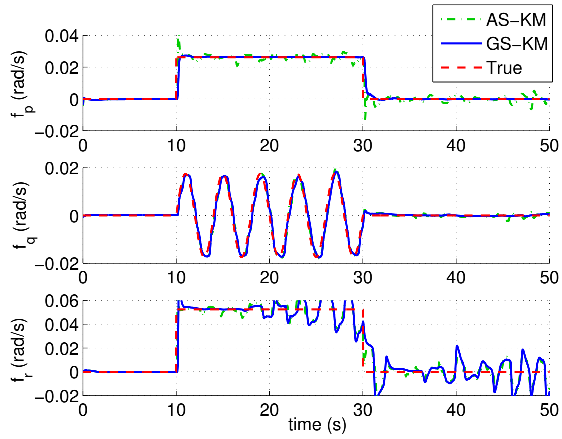

(b) True and estimated f_p, f_q and f_r using the AS-KM and GS-KM

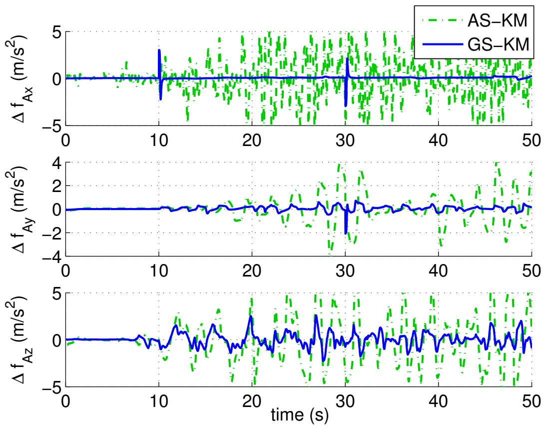

(c) Errors of estimates of f_{Ax}, f_{Ay} and f_{Az} using the AS-KM and GS-KM

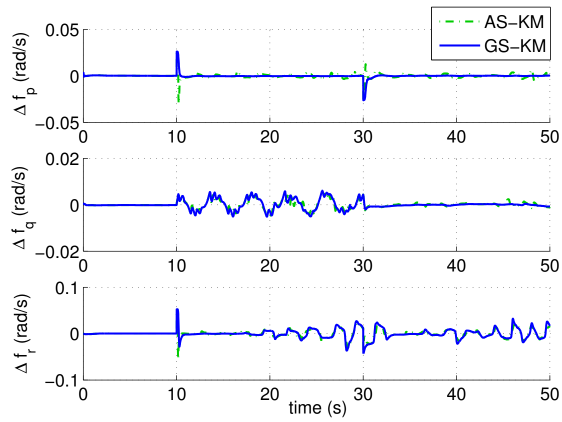

(d) Errors of estimates of f_p, f_q and f_r using the AS-KM and GS-KM

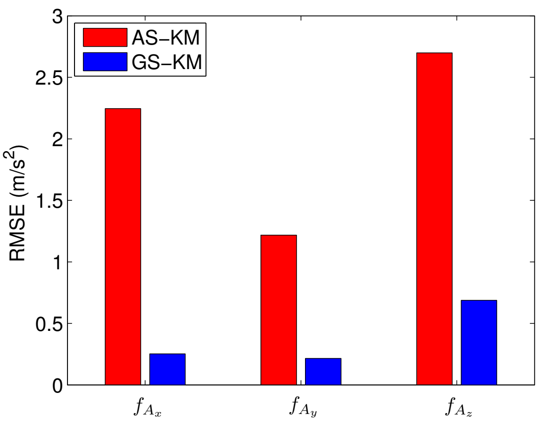

(e) RMSEs of the estimates of f_{Ax}, f_{Ay} and f_{Az}

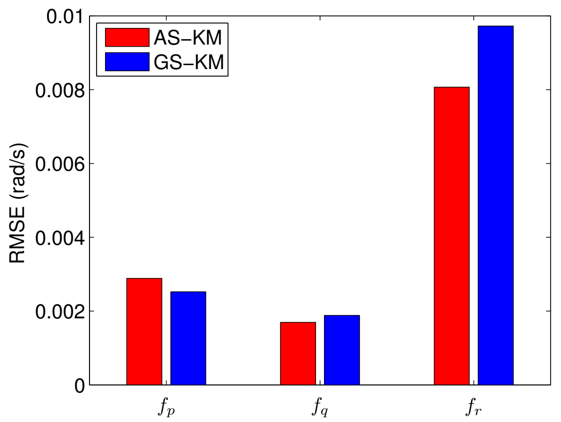

(f) RMSEs of the estimates of f_p, f_q and f_r

Figure 11: Fault estimation results of real flight test scenario 3 (during turbulence)

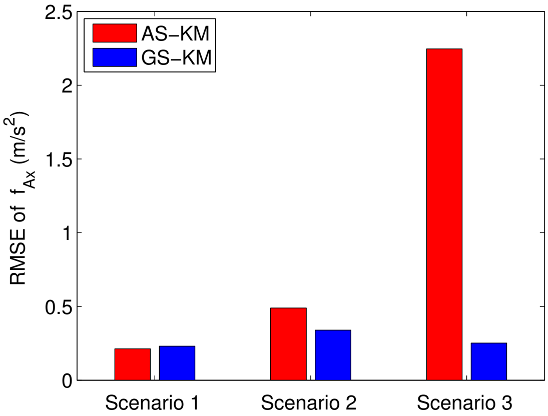

Figure 12: RMSEs of the estimates of f_{Ax} using the AS-KM and GS-KM in the three different flight scenarios

AS-KM is noticeably seen in the figure after $t = 10$ s. The estimates of the ATSEKF using the AS-KM are corrupted by the turbulence, which is similar to those shown in Fig. 5(a). In contrast, the ATSEKF using the GS-KM still maintains satisfactory performance and is significantly better than that using the AS-KM. The fault estimates using the GS-KM can follow the true faults well without being influenced by the turbulence. This clearly demonstrates the superiority of the GS-KM.

The estimates of f_p, f_q and f_r using the two approaches are still comparable, as shown in Fig. 11(b). It shows that although the turbulence can influence the estimation of the accelerometer faults (f_{Ax}, f_{Ay} and f_{Az}), its influence on the estimation of rate gyro faults (f_p, f_q and f_r) is limited.

The fault estimation errors using the two KMs are compared in Fig. 11(c) and 11(d). It is seen that the estimation errors using the GS-KM remain small despite the presence of the turbulence.

The RMSEs of the estimation of f_{Ax}, f_{Ay} and f_{Az} using the two approaches are shown in Fig. 11(e). The RMSEs using the GS-KM are prominently smaller than those using the AS-KM. However, the RMSEs of the estimates of f_p, f_q and f_r using the two approaches are comparable, as shown in Fig. 11(f).

5.4. Discussion on robustness against turbulence

In this section, the robustness of the proposed approach (GS-KM) and the approach using the AS-KM is compared and summarized. Without loss of generality, the RMSE of the estimation of f_{Ax} is taken as an example.

The RMSEs of the estimation of f_{Ax} using the AS-KM and the GS-KM in the three flight scenarios are plotted in Fig. 12. It is evident that the approach using the AS-KM is not robust. The performance changes when the flight scenarios varies. The worst performance occurs when the turbulence is present, which demonstrates that it is sensitive to disturbances. This implies the necessity of considering external disturbances such as turbulence when dealing with aircraft sensor reconstruction.

In contrast, the performance of the proposed approach which uses the GS-KM is more robust to disturbances. The performance does not change significantly even in the presence of turbulence. The performance is notably better than that of using the AS-KM.

Finally, the ground speed measurements are obtained at 1 Hz and are linearly interpolated to obtain data at 100 Hz. To obtain a better performance, ground speed measurements with a high update rate should be applied.

6. Conclusions

This paper proposes a new approach for Inertial Measurement Unit sensor fault reconstruction by making use of the ground-speed-based kinematic model of the aircraft flying in a rotating earth reference frame. Two strategies are proposed for the validation of sensor fault reconstruction approaches: closed-loop and open-loop strategy. Both validation strategies use a newly-developed Adaptive Two-Stage Extended Kalman Filter to estimate the states and faults. The Adaptive Two-Stage Extended Kalman Filter can adaptively update the covariance matrix for fault estimation. The fault reconstruction performance using the ground-speed-based kinematic model is compared to the approach which uses the airspeed-based kinematic model, which shows the performance of the proposed approach.

More importantly, the proposed approach is validated using real flight test data. The performance is tested in various flight conditions and wind conditions including turbulence. The proposed approach is found to be robust in various flight conditions and disturbances such as turbulence, which demonstrates the advantage of the proposed approach.

It is suggested that the proposed approach be incorporated in the aircraft Fault Detection and Isolation and Fault-Tolerant Control systems to enhance the performance of the aircraft.

References

[1] P. Goupil, A. Marcos, The European ADDSAFE project: Industrial and academic efforts towards advanced fault diagnosis, Control Engineering Practice 31 (2014) 109–125.

[2] J. Chen, R. J. Patton, Robust model-based fault diagnosis for dynamic systems, Kluwer Academic Publishers, Norwell, MA, USA, 1999.

[3] R. Isermann, Model-based fault-detection and diagnosis- status and applications, Annual Reviews in Control 29 (2005) 71–85.

[4] V. Venkatasubramanian, R. Rengaswamy, K. Yin, A review of process fault detection and diagnosis Part I : Quantitative model-based methods, Computers and Chemical Engineering 27 (2003) 293–311.

[5] J. Marzat, H. Piet-Lahanier, F. Damongeot, E. Walter, Model-based fault diagnosis for aerospace systems: a survey, Proceedings of the Institution of Mechanical Engineers, Part G: Journal of Aerospace Engineering 226 (2012) 1329–1360.

[6] P. Goupil, J. Boada-bauxell, A. Marcos, P. Rosa, M. Kerr, L. Dalbies, An overview of the FP7 RECONFIGURE project: industrial, scientific and technological objectives, 9th IFAC Symposium on Fault Detection, Supervision and Safety of Technical Processes 48 (2015) 976–981.

[7] A. Marcos, S. Ganguli, G. J. Balas, An application of fault detection and isolation to a transport aircraft, Control Engineering Practice 13 (2005) 105–119.

[8] P. Freeman, P. Seiler, G. J. Balas, Air data system fault modeling and detection, Control Engineering Practice 21 (2013) 1290–1301.

[9] E. Kiyak, A. Kahvecioglu, F. Caliskan, Aircraft Sensor and Actuator Fault Detection, Isolation, and Accommodation, Journal of Aerospace Engineering 24 (2011) 46–58.

[10] P. Castaldi, W. Geri, M. Bonfe, S. Simani, M. Benini, Design of residual generators and adaptive filters for the FDI of aircraft model sensors, Control Engineering Practice 18 (2010) 449–459.

[11] P. Castaldi, N. Mimmo, S. Simani, Differential geometry based active fault tolerant control for aircraft, Control Engineering Practice 32 (2014) 227–235.

[12] H. Alwi, C. Edwards, Development and application of sliding mode LPV fault reconstruction schemes for the ADDSAFE benchmark, Control Engineering Practice 31 (2014) 148–170.

[13] R. C. Avram, X. Zhang, J. Campbell, J. Muse, IMU Sensor Fault Diagnosis and Estimation for Quadrotor UAVs, in: 9th IFAC Symposium on Fault Detection, Supervision and Safety of Technical Processes, volume 48, Elsevier Ltd., 2015, pp. 380–385.

[14] J. Marzat, H. Piet-Lahanier, F. Damongeot, E. Walter, Control-based fault detection and isolation for autonomous aircraft, Proceedings of the Institution of Mechanical Engineers, Part G: Journal of Aerospace Engineering 226 (2011) 510–531.

[15] P. Lu, L. Van Eykeren, E. van Kampen, Q. Chu, Selective-Reinitialisation Multiple Model Adaptive Estimation for Fault Detection and Diagnosis, Journal of Guidance, Control, and Dynamics 38 (2015) 1409–1425.

[16] L. Van Eykeren, Q. Chu, Sensor fault detection and isolation for aircraft control systems by kinematic relations, Control Engineering Practice 31 (2014) 200–210.

[17] P. Lu, L. Van Eykeren, E. van Kampen, C. C. de Visser, Q. Chu, Double-model adaptive fault detection and diagnosis applied to real flight data, Control Engineering Practice 36 (2015) 39–57.

[18] P. Lu, L. Van Eykeren, E. van Kampen, C. C. de Visser, Q. Chu, Adaptive Three-Step Kalman Filter for Air Data Sensor Fault Detection and Diagnosis, Journal of Guidance, Control, and Dynamics (2015) 1–15 (available online).

[19] P. Lu, L. Van Eykeren, E. van Kampen, C. C. de Visser, Q. Chu, Aircraft Inertial Measurement Unit Fault Detection and Diagnosis with Application to Real Flight Data, Journal of Guidance, Control, and Dynamics 38 (2015) 2467–2475.

[20] D. Berdjag, J. Cieslak, A. Zolghadri, Fault diagnosis and monitoring of oscillatory failure case in aircraft inertial system, Control Engineering Practice 20 (2012) 1410–1425.

[21] B. Hu, P. Seiler, Certification Analysis for a Model-Based UAV Fault Detection System, in: AIAA Guidance, Navigation and Control Conference, AIAA 2014-0610, National Harbor, Maryland, 2014, pp. 1–14.

[22] A. Zolghadri, D. Henry, J. Cieslak, D. Efimov, P. Goupil, Fault Diagnosis and Fault-Tolerant Control and Guidance for Aerospace Vehicles, from theory to application, Springer, Series: Advances in Industrial Control, 2013.

[23] P. Goupil, Oscillatory failure case detection in the A380 electrical flight control system by analytical redundancy, Control Engineering Practice 18 (2010) 1110–1119.

[24] C. C. de Visser, J. A. Mulder, Q. Chu, A Multidimensional Spline Based Global Nonlinear Aerodynamic Model for the Cessna Citation II, in: AIAA Atmospheric Flight Mechanics Conference, AIAA 2010-7950, Toronto, Ontario Canada, 2010, pp. 1–30.

[25] L. Van Eykeren, Q. Chu, J. A. Mulder, Sensor Fault Detection and Isolation using Adaptive Extended Kalman Filter, in: 8th IFAC Symposium on Fault Detection, Supervision and Safety of Technical Processes, 1969, Mexico, 2012, pp. 1155–1160.

[26] P. Lu, E. van Kampen, Aircraft Inertial Measurement Unit Fault Identification with Application to Real Flight Data, in:

AIAA Guidance, Navigation and Control Conference, AIAA 2015-0859, Kissimmee, Florida, 2015, pp. 1–17.

[27] J. Mulder, Q. Chu, J. Sridhar, Non-linear aircraft flight path reconstruction review and new advances, Progress in Aerospace Sciences 35 (1999) 673–726.

[28] D. Mclean, Automatic Flight Control Systems, Englewood Cliffs, NJ: Prentice-Hall, 1990.

[29] D. Bates, M. Hagström, Nonlinear Analysis and Synthesis Techniques for Aircraft Control, Springer-Verlag Berlin Heidelberg, 2007.

[30] C.-S. Hsieh, F.-G. Chen, Optimal Solution of the Two-Stage Kalman Estimator, IEEE Transactions on Automatic Control 44 (1999) 194–199.

[31] R. K. Mehra, Approaches to adaptive filtering, IEEE Transactions on Automatic Control 17 (1972) 693–698.

[32] R. Sreedhar, B. Fernandez, G. Y. Masada, Robust Fault Detection in Nonlinear Systems Using Sliding Mode Observers, in: Second IEEE Conference on Control Applications, 2, Vancouver, BC, 1993, pp. 715–721.

[33] C. Edwards, S. Spurgeon, R. Patton, Sliding mode observers for fault detection and isolation, Automatica 36 (2000) 541–553.